remote sensing

MDPI

Article

Calibration and Validation of NOAA-21 Ozone Mapping and Profiler Suite (OMPS) Nadir Mapper Sensor Data Record Data

Banghua Yan [1,*], Trevor Beck [1], Junye Chen [2], Steven Buckner [2], Xin Jin [2], Ding Liang [2], Sirish Uprety [3], Jingfeng Huang [4], Lawrence E. Flynn [1], Likun Wang [3], Quanhua Liu [1] and Warren D. Porter [2]

[1] NOAA Center for Satellite Applications & Research, College Park, MD 20740, USA; trevor.beck@noaa.gov (T.B.); lawrence.e.flynn@noaa.gov (L.E.F.); quanhua.liu@noaa.gov (Q.L.)
[2] ERT, Inc., 14401 Sweitzer Lane Suite 300, Laurel, MD 20707, USA; junye.chen@noaa.gov (J.C.); steven.buckner@noaa.gov (S.B.); xin.jin@noaa.gov (X.J.); ding.liang@noaa.gov (D.L.); warren.porter@noaa.gov (W.D.P.)
[3] ESSIC/CISESS, University of Maryland, College Park, MD 20740, USA; sirish.uprety@noaa.gov (S.U.); likun.wang@noaa.gov (L.W.)
[4] Science Systems and Applications, Inc., Lanham, MD 20706, USA; jingfeng.huang@ssaihq.com
* Correspondence: banghua.yan@noaa.gov; Tel.: +1-301-683-3602

Abstract: The Ozone Mapping and Profiler Suites (OMPS) Nadir Mapper (NM) is a grating spectrometer within the OMPS nadir instruments onboard the SNPP, NOAA-20, and NOAA-21 satellites. It is designed to measure Earth radiance and solar irradiance spectra in wavelengths from 300 nm to 380 nm for operational retrievals of the nadir total column ozone. This study presents calibration and validation analysis results for the NOAA-21 OMPS NM SDR data to meet the JPSS scientific requirements. The NOAA-21 OMPS SDR calibration derives updates of several previous OMPS algorithms, including the dark current correction algorithm, one-time wavelength registration from ground to on-orbit, daily intra-orbit wavelength shift correction, and stray light correction. Additionally, this study derives an empirical scale factor to remove 2.2% of systematic biases in solar flux data, which were caused by pre-launch solar calibration errors of the OMPS nadir instruments. The validation of the NOAA-21 OMPS SDR data is conducted using various methods. For example, the 32-day average method and radiative transfer model are employed to estimate inter-sensor radiometric calibration differences from either the SNPP or NOAA-20 data. The quality of the NOAA-21 OMPS NM SDR data is largely consistent with that of the SNPP and NOAA-20 OMPS data, with differences generally within ±2%. This meets the scientific requirements, except for some deviations mainly in the dichroic range between 300 nm and 303 nm. The deep convective cloud target approach is used to monitor the stability of NOAA-21 OMPS reflectance above 330 nm, showing a variation of 0.5% over the observed period. Data from the NOAA-21 VIIRS M1 band are used to estimate OMPS NM data geolocation errors, revealing that along-track errors can reach up to 3 km, while cross-track errors are generally within ±1 km.

Keywords: NOAA-21 OMPS; Nadir Mapper (NM); calibration and validation; dark current correction; wavelength registration; intra-orbit wavelength shift correction; stray light correction; geolocation accuracy; inter-sensor comparison; 32-day average method; double differences via radiative transfer model; deep convective cloud target approach

check for updates

Citation: Yan, B.; Beck, T.; Chen, J.; Buckner, S.; Jin, X.; Liang, D.; Uprety, S.; Huang, J.; Flynn, L.E.; Wang, L.; et al. Calibration and Validation of NOAA-21 Ozone Mapping and Profiler Suite (OMPS) Nadir Mapper Sensor Data Record Data. *Remote Sens.* **2024**, *16*, 4488. https://doi.org/10.3390/rs16234488

Academic Editors: Raad A. Saleh, Yonghua Jiang, Mingjun Deng and Litao Li

Received: 17 September 2024
Revised: 4 November 2024
Accepted: 19 November 2024
Published: 29 November 2024

Copyright: © 2024 by the authors. Licensee MDPI, Basel, Switzerland. This article is an open access article distributed under the terms and conditions of the Creative Commons Attribution (CC BY) license (https://creativecommons.org/licenses/by/4.0/).

1. Introduction

The Ozone Mapping and Profiler Suites (OMPS) [1–3] are an important payload onboard the SNPP, NOAA-20, and NOAA-21 satellites, which were launched on 28 October 2011, 18 November 2017, and 10 November 2022, respectively. The Nadir Mapper (NM) and Nadir Profiler (NP) within the OMPS are two grating spectrometers designed to measure Earth radiance and solar irradiance spectra in the UV bands. In operational products, the NM covers wavelengths from 300 nm to 380 nm for observations of the nadir total column

ozone [4], while the NP covers wavelengths from 250 nm to 310 nm for observations of ozone vertical distributions [5]. The Limb profiler, the third spectrometer within the SNPP and NOAA-21 OMPS, measures scattering radiance from the Earth limb [6], but is not included in NOAA OMPS SDR calibration activities. Therefore, for simplification, OMPS sensors hereinafter refer only to the NM and NP. Currently, the OMPS SDR data from SNPP and NOAA-20 satellites are widely used to produce a series of well-calibrated EDR products, such as the total column ozone, vertical profile of ozone, aerosol index, and SO_2, referring to [7–11]. Additionally, experimental OMPS NM SDR radiance assimilation has been demonstrated through one-dimensional variational analysis [12], showing promising results for assimilating OMPS SDR data into NWP models. SNPP OMPS NM and NP SDR data have been reprocessed to produce a mission-long calibration-consistent data record [13], while NOAA-20 OMPS SDR data reprocessing is also planned. As the latest unit in the OMPS series, the NOAA-21 OMPS NM and NP SDR data not only ensure the continuation of these applications but also enable a longer ozone data record. Therefore, it is crucial to thoroughly calibrate and validate the NOAA-21 OMPS NM and NP SDR data to meet the scientific requirements. Due to many abbreviations, a list of abbreviations is included in Table A1 in Appendix A.

Over the past decade, intensive studies have been conducted to develop calibration algorithms for dark current correction, wavelength registration, wavelength shift correction, stray light correction, and geolocation registration for SNPP and NOAA-20 OMPS SDR data [14–25]. These high-level principles are applicable for NOAA-21 OMPS SDR data. However, the OMPS instruments on the SNPP, NOAA-20, and NOAA-21 satellites have not been characterized consistently. Discrepancies in pre-launch instrument characterizations exist among the three OMPS instruments, such as spectral response characteristics, radiance (solar irradiance) calibration coefficients, polarization sensitivity, and the stray light-relevant point spread function (PSF). In addition, significant deviations in measured NOAA-21 OMPS reflectance were reported in early-orbit data analysis [26,27]. The problem was caused by pre-launch solar flux calibration errors [a personal communication with G. Jaross of NASA]. As a result, the NOAA-21 OMPS instrument exhibits different on-orbit spectral features in various aspects, such as the wavelength shift, stray light, dark current, geolocation accuracy, and SNR, compared to the SNPP and NOAA-20 instruments. These challenges necessitate updating existing calibration algorithms from the SNPP and NOAA-20 to the NOAA-21 OMPS instrument. Therefore, a series of existing calibration algorithms for the NOAA-21 OMPS SDR have been updated through activities carried out through three scientific reviews, progressing from beta, provisional, to validated maturity levels [26,28–30]. The final review, achieving validated maturity, indicates that the updated algorithms can generally ensure the SDR data quality meets the scientific requirements defined in the JPSS mission [31,32].

This study presents our analysis results on the calibration and validation of the NOAA-21 OMPS NM SDR data at a validated maturity level. A separate manuscript will address the analysis of the NOAA-21 OMPS NP SDR data. The calibration procedures used in this study have been established with previous OMPS NM instruments. This study focuses on the updates of the calibration algorithms, including the dark current correction, one-time wavelength registration from ground to on-orbit, and orbital intra-orbit wavelength shift correction. Additionally, a new empirical approach is developed to mitigate impact of solar flux pre-launch calibration errors. The impact of the stray light correction algorithm is introduced, but its detailed derivation and performance will be provided in a separate manuscript [33] to avoid an overly lengthy manuscript. These updated calibration algorithms have been implemented into the JPSS IDPS processing system through calibration tables or code change to generate operational OMPS SDR data. Consequently, the accuracy of those calibration algorithms directly determines the accuracy of the NOAA-21 OMPS NM SDR data. In this study, the radiometric and geolocation quality of the NOAA-21 OMPS are validated using various methods. For instance, radiance and reflectance in the SDR data are validated primarily by assessing inter-sensor radiometric calibration biases with the SNPP

and NOAA-20. This inter-sensor analysis employs an existing 32-day average method [34] and a double-difference (DD) method via an RTM as a bridge (i.e., the RTM-DD). Moreover, the DCC target method [35,36] was used to assess the long-term stability of the NOAA-21 OMPS NM SDR data at wavelengths above 330 nm. The geolocation accuracy of the OMPS NM SDR data is analyzed against NOAA-21 VIIRS observations at the M1 band, as we did for the SNPP and NOAA-20 [25]. The SNR performance of the OMPS SDR data is calculated by using a statistical method.

Note that this manuscript centers on the enhancements to the existing algorithms. The original OMPS SDR calibration algorithms were introduced more than two decades ago, with details provided in a series of publications listed in the references (e.g., [1–9,13–24]). Subsequent updates to the NOAA-21 OMPS NM SDR calibration algorithms were also progressively finalized through three scientific review stages, i.e., the beta maturity review [28], the provisional maturity review [26], and the validated maturity review [29]. These reviews assessed accuracy improvement before and after the updates. To maintain the manuscript conciseness, this study excludes results based upon pre-launch calibration tables or outdated algorithms. For comprehensive information on the original OMPS calibration algorithms, and before-and-after comparisons following the latest updates, which are used in this study, please refer to the cited reviews and publications.

This paper is organized as follows. Section 2 introduces the NOAA-21 OMPS NM instrument, its requirements, and SDR data access. Section 3 delineates the updated OMPS NM SDR calibration algorithms for the NOAA-21 OMPS. It also includes an empirical approach to derive a scale factor for mitigating solar flux errors. Section 4 evaluates the radiometric and geolocation quality of the NOAA-21 OMPS NM SDR data, including Earth radiance, reflectance, SNR, and geolocation. Section 5 offers a summary and concluding remarks.

2. OMPS NM Instrument, SDR Product Requirements, and Data Access

2.1. OMPS NM Instrument

The detailed descriptions of the OMPS instrument were given in previous studies [4,5,18,19]. Below, a briefing is given.

The OMPS nadir instrument is an important payload onboard the SNPP, NOAA-20, and NOAA-21 satellites. Its optomechanical design is modular, consisting of the telescope, and NM and NP spectrometers. The telescope feeds the entrance slits of the two spectrometers and has a 110° cross-track field of view [1]. Following the imaging optics are a dichroic beam splitter that is optimized to reflect most of the 250–310 nm light to the profile spectrometer and transmit most of the 300–380 nm light to the total column spectrometer [1]. Notice that a common wavelength range exists during wavelengths from 300 nm to 310 nm, where the reflectance to the Nadir Profiler goes from close to 100% near 300 nm to close to 0% near 310 nm. This range is defined as the transition range of the dichroic or the dichroic (transition) range.

The NOAA-21 OMPS instrument was designed with similar characterization specifications as its two predecessors, the SNPP and NOAA-20, except for a large difference in spatial resolution. Operational OMPS NM data cover the wavelength from 300 to 380 nm for ozone total column observations with a changeable channel number with the satellite. The OMPS instrument focal plane was designed to have a 1.1 nm FWHM and 0.42 nm sampling. The IFOV at nadir varies with each satellite, resulting in different spatial resolutions for each NM sensor. Table 1 summarizes the OMPS NM and NP instrument specification characteristics.

The OMPS instrument consists of the following two observation scanning modes: earth observation and solar diffuser calibration view mode.

For the Earth radiance scanning mode, observations from the NM are collected over a full 110° cross-track across a 2800 km Earth-view swath, which are saved by a CCD located at the spectrometer's focal plane [1]. The NM FPAs consist of dual 2D CCD optical detectors to provide a response to photons within its spectral and spatial ranges [1,18]. Each CCD

image consists of 340 micropixels (CCD cells) along the spectral dimension and 740 micropixels in the spatial dimension. For the NOAA-21 OMPS NM, only 198 spectral channels out of the full 340 CCD spectral dimension are used, ranging from index 45 to index 242, and 709 pixels (cell)s out of the 740 full CCD spatial dimension are used, ranging from index 16 to index 724. Additionally, in the IDPS operational processing, 709 spatial CCD cells are aggregated to form a small number of macropixels with the required spatial resolution. For example, in the case of the NOAA-21 OMPS, 709 CCD micropixels are aggregated into 177 macropixels, corresponding to 177 FOV positions (pixels). The nadir FOV pixel has a spatial resolution of 12 km in the cross-track direction and 10 km in the along-track direction (see the highlighted spatial resolution in blue in Table 1). There is no aggregation for the spectral cells, resulting in the abovementioned 198 wavelength channels. However, the central wavelength at each channel can slightly vary with each scan (latitude) due to the OMPS nadir calibration and NM housing temperature gradients (see Section 3.4.2 for details).

Table 1. OMPS NM and NP instrument specification characteristics [4,5,19].

Sensor Name	**Nadir Mapper (NM)**			**Nadir Profiler (NP)**		
Spectrometer Type	Grating spectrometer			Double-grating spectrometer		
Sensor View Angle Range	110° cross-track			Nadir view (16.7°), 50 km cross-track		
Spectral Range (nm)	300~380			250~310		
FWHM Bandpass (nm) Spectral Sampling (nm)	1.1 0.42			1.1 0.42		
Spatial Resolution [1] at Nadir (km^2)	NPP: 50 × 50	N20: 50 × 17	N21: 12 × 10	NPP: 250 × 250	N20: 50 × 50	N21: 50 × 50
Channel	NPP: 196	N20: 196	N21: 198	NPP: 147	N20: 151	N21: 158

Note: [1] NPP, N20, and N21 denote SNPP, NOAA-20, and NOAA-21, correspondingly. The Nadir Profiler footprint covers a 250 km cross-track for all instruments. The pixel size does vary between instruments.

Solar observations for the calibration mode are conducted using the following two diffusers: a reflective working diffuser, used bi-weekly for short-term monitoring, and a reflective reference diffuser, used every six months or one year for long-term monitoring of sensor stability. As described in [18], during each solar measurement, the diffuser moves through seven different positions to cover the entire 110° FOV of the NM sensor. For the NOAA-21 OMPS nadir instrument, the entire sequence of solar measurements is performed near the Northern Earth Terminator, with solar zenith angles of 80° to 100°, to produce a series of CCD images.

2.2. OMPS NM SDR Specification Requirements

The requirements for the NOAA-21 are the same as those for the NOAA-20, except for the SNR due to a high spatial resolution. Table 2 summarizes the requirements for the NOAA-21 OMPS NM SDR data based on JPSS program documentation [31,32]. These requirements, except for stray light, will be reflected in either Section 3 or Section 4 below.

Table 2. The requirements of the NOAA-21 OMPS NM SDR products [31,32].

Variable	**Requirement**
SNR radiance @17 km × 17 km [1]	>195 (305–380 nm)
Irradiance uncertainty	<7%
Wavelength registration accuracy	<0.01 nm
Intra-orbital wavelength variation	<0.01 nm
Radiance uncertainty	<8%
OOB stray light	≤10%
Maximum albedo calibration	<2%
Geolocation error	≤8.5 km @nadir (AT)

Note: [1] SNR requirements are defined only at wavelengths above 305 nm.

2.3. Data Access

The NOAA-21 OMPS SDR data used in this study are routinely produced in the IDPS operational processing system at the NOAA ESPC. Near-real time SDR data are distributed through the PDA system (https://espdsport-dmz.espc.nesdis.noaa.gov/PdaUserPortal, accessed on 15 April 2023; an account and connecting to the ESPC VPN are required), the JPSS GRAVITE system (https://gravite.jpss.noaa.gov/, accessed on 18 January 2023) [37], and the NOAA Direct Readout [38]. Long-term access to OMPS SDR data is available in the CLASS (https://www.aev.class.noaa.gov/saa/products/welcome, accessed on 15 April 2023). The solar flux data used in this study are from the solar flux L1B data per image in the NASA SIPS website (https://omisips1.omisips.eosdis.nasa.gov/sipslogin.md, accessed on 18 February 2023), which are calibrated by the NASA OMPS group.

3. Updates of Calibration Algorithms for NOAA-21 OMPS NM

Each calibration algorithm for the NOAA-21 OMPS NM is used to execute specific functions within the OMPS radiometric calibration methodology. Hence, the OMPS radiometric calibration methodology is introduced before discussing several calibration algorithms.

3.1. OMPS Radiometric Calibration Methodology

The OMPS SDR calibration methodology consists of Earth radiance and solar irradiance calibrations, as well as an important derived quantity, the reflectance or normalized radiance (*NR*). The following radiance and irradiance equations are given in the single CCD cell (micropixel), avoiding complication in the aggregation of a variable index in the spatial domain. The radiance and irradiance equations at the macropixel level, resulting from the aggregation of several CCD cells in the spatial direction according to the OMPS sample table, can be referenced in [24].

The Earth radiance calibration for a single pixel $(j,\ l)$ is expressed as a function of the corrected radiance counts C^r_{jl} included in the OMPS RDR data by [3,5,18], as follows:

$$I^m_{jl}(t) = \frac{C^r_{jl} k^r_{jl}}{\tau_{jl}(t)}, \tag{1}$$

where C^r_{jl} is an offset-corrected radiance count; k^r_{jl} is a calibration coefficient determined during pre-launch calibration; $\tau_{jl}(t)$ represents a sensor response change as a function of time t, $with\ \tau_{jl}(t=0) = 1$; the subscript indices j and l correspond to the spatial and spectral dimensions in a CCD image, respectively. The specific wavelength and spatial geolocation with respect to the two indices are determined by the spectral wavelength and spatial registrations separately (see Sections 3.4 and 3.6 below). The explanations of the variables in Equation (1) and other equations in this study are summarized in Table 3.

Table 3. Physical explanations of variables in Equation (1) and the other equations in this study.

Variable	Explanation
$I^m_{jl}(t)$	calibrated Earth radiance for pixel (j,l), with a spectral pixel index of j and a spatial pixel index of l
$F^m_{jl}(t)$	calibrated solar irradiance for pixel (j,l)
$NR^m_{jl}(t)$	normalized radiance
C^r_{jl}	offset-corrected Earth radiance counts for pixel (j,l)
C^i_{jl}	corrected solar irradiance counts for pixel (j,l)
k^r_{jl}	pre-launch measured radiance calibration coefficient for pixel (j,l)
k^i_{jl}	pre-launch measured irradiance calibration coefficient for pixel (j,l)

Table 3. *Cont.*

Variable	Explanation
K_{jl}	combined calibration constant for normalized radiance
$\tau_{jl}(t)$	sensor response changes as a function of time t
$g_{jl}(\theta, \varphi)$	pre-launch relative angular irradiance response (goniometric) of the sensor at solar angle (θ, φ)
$\rho_{jl}(t)$	solar diffuser plate reflectivity change
C_{jl}	correct counts for a pixel (j, l), which is applicable for both C^r_{jl} and C^i_{jl}
O_{jl}	nonlinearity-corrected counts for either radiance or solar irradiance at a pixel (j, l)
S_{jl}	observational smear
D_{jl}	CCD dark current that is subject to bias correction

The solar irradiance calibration is expressed as

$$F^m_{jl}(t) = \frac{C^i_{jl} k^i_{jl}}{\tau_{jl}(t) g_{jl}(\theta, \varphi) \rho_{jl}(t)}, \tag{2}$$

where C^i_{jl} is an offset-corrected irradiance count; $g_{jl}(\theta, \varphi)$ denotes the sensor's relative angular irradiance response (goniometric) at solar angles (θ, φ), where θ and φ denote the SZA and azimuthal angle, respectively; $\rho_{jl}(t)$ is the solar diffuser plate reflectivity change, with $\rho_{jl}(t = 0) = 1$. The calibration coefficients, k^i_{jl}, and $g_{jl}(\theta, \varphi)$, are determined during the pre-launch calibration. These coefficients were normally well calibrated, with an exception in k^i_{jl} for NOAA-21 OMPS. The pre-launch albedo calibration of the NOAA-21 OMPS was reported to have errors of several percent, varying by wavelength, either in the OMPS response or in the solar irradiance calibrations [courtesy of Jaros G. in the NASA for an email communication in 2024]. However, accurate pre-launch calibration errors are not well understood. Consequently, no error-corrected calibration coefficients are available for use in the post-calibration of solar flux. This issue has significantly impacted the OMPS SDR normalized radiance accuracies, leading to the development of an empirical solar flux error correction factor (refer to Section 3.2 below).

Then, the normalized radiance (*NR*), $NR^m_{jl}(t)$, is defined by

$$NR^m_{jl}(t) = \frac{I^m_{jl}(t)}{F^m_{jl}(t)} = K_{jl} \frac{C^r_{jl}}{C^i_{jl}} g_{jl}(\theta, \varphi) \rho_{jl}(t), with\ K_{jl} = \frac{k^r_{jl}}{k^i_{jl}}, \tag{3}$$

where the sensor response change is cancelled through the ratio since the sensor response change affects both the Earth radiance and solar irradiances. The logarithm of this quantity has a scaling comparable to the total column ozone, while the reflectance is almost identical to the *NR* except for an adjustment by $\frac{1}{coscos\ (\theta)}$. Thus, the normalized radiance is frequently used to replace reflectance in this study.

In Equations (1)–(3), both C^r_{jl} and C^i_{jl} represent the offset-corrected radiometric counts for radiance and irradiance at a pixel (j, l), such as corrections of the dark current, smear, and stray light. For the OMPS observations, the nonlinearity is caused by imperfect gain responses of on-chip CCD amplifiers within the instrument. Its correction for NOAA-21 instrument has been performed in the OMPS flight software FSW7.3, so the nonlinearity correction is not explicated here. Offset-corrected counts are expressed in a common equation, i.e.,

$$C_{jl} = O_{jl} - D_{jl} - SL_{jl} - S_{jl} \tag{4}$$

where C_{jl} represents an offset-corrected count for a pixel (j, l), which is applicable for both C^r_{jl} and C^i_{jl}; O_{jl} denotes the nonlinearity-corrected count for either radiance or solar

irradiance at a pixel (j,l); SL_{jl} denotes the received stray light at (j,l), which is related to the OOB and OOF stray light (SL) contributions; S_{jl} denotes the smear after corrections for electronic bias and dark current, resulting from the photon flux incident upon the pixels during the parallel charge transfer operations; D_{jl} represents the CCD dark current that is subject to bias corrections (see Section 3.3 below for details).

According to Equations (1)–(4), the calibration accuracies of radiance, irradiance, and *NR* are primarily determined by accuracies in the calibration parameters or indices in Equations (1)–(4). This process is performed though individual calibration algorithms, e.g., the spectral wavelength registration associated with the index l for the variables, the geolocation spatial registration associated with the index j, the SL correction as described in SL_{jl} in Equation (4), and the dark current correction [see D_{jl} in Equation (4)]. Several standard algorithms had been well developed for the SNPP and NOAA-20 OMPS to execute those functions. Those algorithms need to be updated to NOAA-21 to ensure the NOAA-21 OMPS NM SDR data meet the requirements. In addition, a new empirical scale factor is derived to remove major solar flux errors in the NOAA-21 OMPS, which is described first in the following analyses.

3.2. Correcting for Pre-Launch Solar Calibration Errors

The impacts of solar flux errors were reported from the NOAA-21 OMPS NM and NP during their initial orbit calibration analyses [26,27,29]. An empirical approach is presented below to derive a scale factor to reduce major calibration biases in the NOAA-21 OMPS NM day-1 solar spectrum by using the SNPP as a reference.

Calibration errors relative to the SNPP are quantified by calculating the double-difference between the synthetic solar spectrum and the day-1 solar spectrum for both the SNPP and NOAA-21 OMPS NM. For convenience, $DD^{Solar}_{N21-SNPP}$ is introduced to represent this double difference, as described below:

$$DD^{Solar,NoCor}_{N21-SNPP} = \Delta^{Solar}_{N21} - \Delta^{Solar}_{SNPP} \tag{5}$$

$$\Delta^{Solar}_{N21} = F^{Syn}_{N21}(\lambda) - F^{Day1}_{N21}(\lambda) \tag{6}$$

$$\Delta^{Solar}_{SNPP} = F^{Syn}_{SNPP}(\lambda) - F^{Day1}_{SNPP}(\lambda) \tag{7}$$

where $DD^{Solar,NoCor}_{N21-SNPP}$ is the double difference in Δ^{Solar}_{N21} and Δ^{Solar}_{SNPP}; Δ^{Solar}_{N21} and Δ^{Solar}_{SNPP} denote the difference in the synthetic solar spectrum from the day-1 solar spectrum for the NOAA-21 and SNPP, respectively; the superscript 'NoCor' denotes that the double difference is carried out in the absence of the pre-launch calibration error correction.

To clarify the rationale behind the double-difference approach, Equation (5) is rewritten as follows:

$$DD^{Solar,NoCor}_{N21-SNPP} = -\left[F^{Day1}_{N21}(\lambda) - F^{Day1}_{SNPP}(\lambda)\right] + \left[F^{Syn}_{N21}(\lambda) - F^{Syn}_{SNPP}(\lambda)\right] \tag{8}$$

Mathematically, if the OMPS nadir instrument spectral response features are the same for both the SNPP and NOAA-21, we have $F^{Syn}_{N21}(\lambda) = F^{Syn}_{SNPP}(\lambda)$ because both $F^{Syn}_{SNPP}(\lambda)$ and $F^{Syn}_{N21}(\lambda)$ are computed using the same hyperspectral solar reference dataset. Under this condition, the second item in Equation (8) is zero. In other words, $DD^{Solar,NoCor}_{N21-SNPP}$ is identical to the difference in the two day-1 solar spectra. However, for the actual SNPP and NOAA-21 OMPS nadir instruments, $F^{Syn}_{N21}(\lambda)$ shows an order of 1% differences within the range from 300 nm to 310 nm due to different spectral response features. This difference will be transferred to the difference in the two day-1 spectra through on-orbit measurements of solar flux by each individual OMPS sensor. The double difference via Equation (5) is thus designed to reduce this impact due to two OMPS sensors' spectral response feature differences. The SNPP OMPS SDR data have been well calibrated [14–18]. Therefore, $DD^{Solar,NoCor}_{N21-SNPP}$ is determined primarily by NOAA-21 calibration errors.

Figure 1a,b display Δ_{SNPP}^{Solar} and Δ_{N21}^{Solar}, respectively, as a function of wavelength. For the SNPP OMPS NM, the magnitudes of Δ_{SNPP}^{Solar} typically fall within ±2.5% across the entire wavelength range. The mean difference is only about 0.07%. This small systematic bias implies that the SNPP OMPS NM does not have obvious pre-launch calibration errors in the solar irradiance. Hence, it is reasonable to use the SNPP as a reference in this analysis. In contrast with Δ_{SNPP}^{Solar}, Δ_{N21}^{Solar} in Figure 1b exhibits a relatively large variation, with a more than 2% systematic bias. Those results indicate that $DD_{N21-SNPP}^{Solar,NoCor}$ is dominated by NOAA-21 OMPS pre-launch calibration errors. Additionally, the small-scale fluctuation structure in Figure 1b is very similar to Figure 1a, indicating that two OMPS NM sensors exhibit similar changes from ground to flight in the spectral wavelength scale and other spectral features.

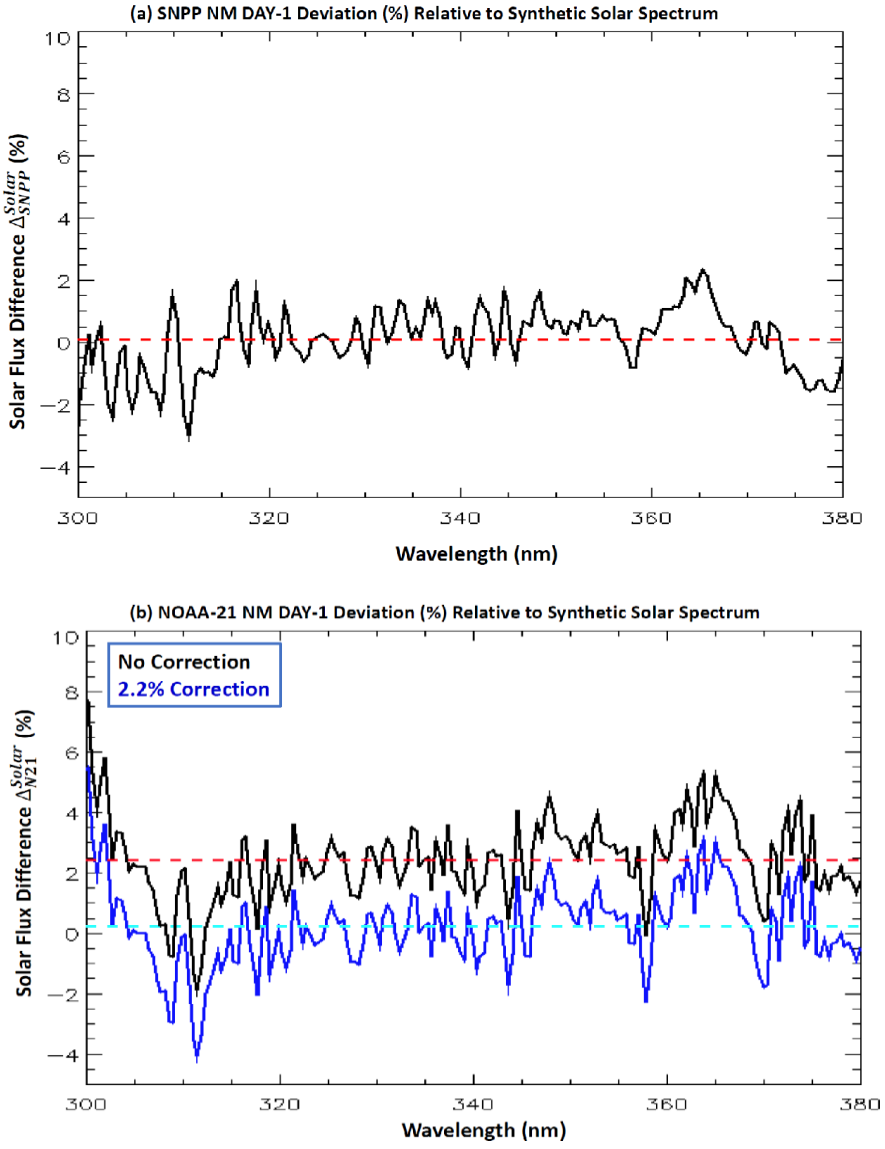


Figure 1. *Cont.*

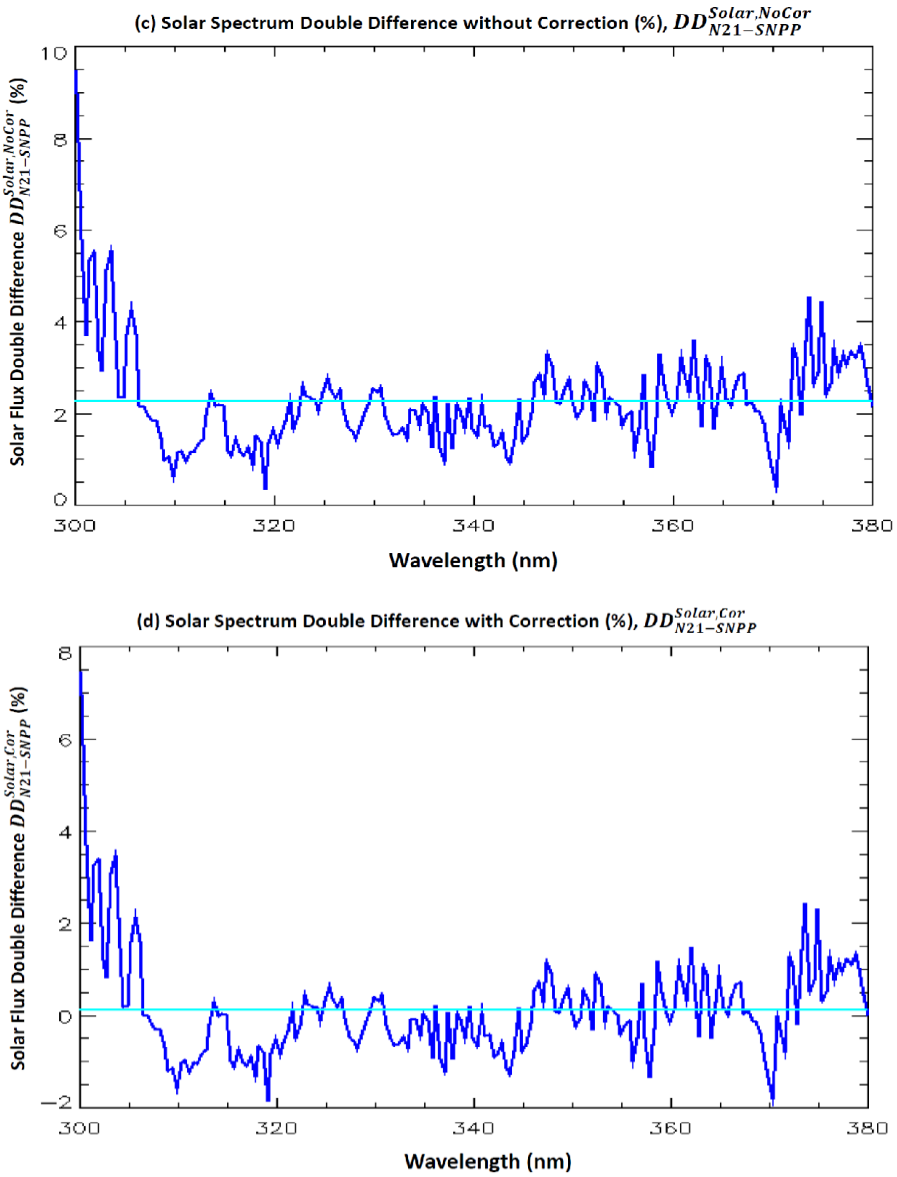


Figure 1. Deviation of the on-board-measured (day-1) solar spectrum from the pre-launch instrument-based (synthetic) solar spectrum for both the SNPP and NOAA-21 OMPS NM, respectively, i.e., Δ^{Solar}_{N21} and Δ^{Solar}_{SNPP}, and their double differences with/without the solar calibration corrections, i.e., $DD^{Solar,\ NoCor}_{N21-SNPP}$ and $DD^{Solar,\ Cor}_{N21-SNPP}$. In (**a**,**b**), the red dash line represents the average values of Δ^{Solar}_{SNPP} and Δ^{Solar}_{N21}, respectively. Additionally, the results of Δ^{Solar}_{N21} after applying the 2.2% correction is included in (**b**), with the light blue dash line indicating their average value. (**a**) Δ^{Solar}_{SNPP}; (**b**) Δ^{Solar}_{N21}; (**c**) $DD^{Solar,NoCor}_{N21-SNPP}$; (**d**) $DD^{Solar,Cor}_{N21-SNPP}$.

To derive the correction factor for the NOAA-21 OMPS NM solar errors, Figure 1c displays the double difference in two individual differences without error corrections in the NOAA-21 NM day-1 solar spectrum, i.e., $DD^{Solar,NoCor}_{N21-SNPP}$, while the $DD^{Solar,NoCor}_{N21-SNPP}$ exhibits a strong wavelength dependency especially in the dichroic range, where the double differences are the largest. The wavelength dependency beyond the dichroic range is caused partially by NOAA-21 OMPS pre-launch calibration errors, which was also reported by the OMPS instrument vendor. Within the dichroic range, the $DD^{Solar,NoCor}_{N21-SNPP}$ shows the strongest dependency upon the wavelength, while the magnitudes are the largest. This feature is attributed to relatively large changes in the SNPP and NOAA-21 instrument spectral features from ground to orbit, which are observed in Figure 1a,b. Firstly,

we use pixel-based calibration coefficients in the OMPS SDR calibration algorithm. The coefficients not only have a large gradient in this wavelength transition range but can also be changed with both the instrument operating temperature and outgassing of water vapor after the instrument is in flight. Currently, changes in coefficients from ground to orbit have not been well understood due to the lack of the truth. As a result, changes in the radiometric calibration coefficients from ground to orbit are not accounted for in the OMPS SDR data processing. Secondly, the dichroic range can be shifted when the OMPS sensor is transitioned from ground to orbit. This shift adds further uncertainties to the radiance calibration coefficients within the dichroic range, even though the wavelength shift from ground to orbit has been approximately estimated and corrected (see Section 3.4 below).

In addition to the wavelength dependency, a mean difference of over 2% persists between Δ_{N21}^{Solar} and Δ_{SNPP}^{Solar}. This systematic error is primarily pertinent to the pre-launch solar calibration errors in the NOAA-21 OMPS NM, as the wavelength-averaged difference in Δ_{SNPP}^{Solar} is only about 0.07%. Specifically, an averaged bias between Δ_{N21}^{Solar} and Δ_{SNPP}^{Solar}, at 2.2%, is derived, which is an average of all $DD_{N21-SNPP}^{Solar,NoCor}$ values after excluding a few extreme cases below 301 nm. Therefore, this 2.2% is used as a scale factor to reduce major errors in the NOAA-21 OMPS in-flight solar flux data against the SNPP. The results of Δ_{N21}^{Solar}, following a 2.2% correction, are added in Figure 1b (see blue line), while the newly computed double differences with the bias correction, $DD_{N21-SNPP}^{Solar,Cor}$, are shown in Figure 1d. The new averages in both Δ_{N21}^{Solar} and $DD_{N21-SNPP}^{Solar,Cor}$ are approximately within 0.1% of the zero line, confirming the effective performance of this empirically derived bias correction scale factor.

3.3. Dark Calibration

Theoretically, dark current is the unwanted electrical current that flows through a photon collection device, typically due to thermal energy, adding unwanted counts to the photon-generated pixel counts. For the OMPS measurements, the radiometric counts for Earth data in Equation (4) are affected by dark current during the readout time period, when the Earth radiometric counts are transferred from the image region to the storage region. Therefore, one important calibration is to correct the counts due to dark current. A schematic diagram of the OMPS dual CCD readout full-frame image format was described in [17]. In the operational OMPS SDR processing, this process is performed at a macropixel with the following equation [5,13,14,17,39]:

$$D_{Jl} = \sum_{j=N_D}^{N_j} \frac{t_E}{t_D} \left(D_{jl}^{Obs} - B_D \right) \tag{9}$$

where D_{jl}^{Obs} is an observed dark count without correction; B_D denotes the bias for the dark data, which is determined by the readout time and dark storage rate; j denotes the jth CCD micropixel; J is the Jth macropixel, including micropixels between indices from N_D to N_j; t_E and t_D are the integration time for the Earth and dark data, respectively.

In the computation of D_{Jl}, D_{jk}^{Obs} is determined by the image region dark rate and integration time. About a decade ago, a well-validated processing package, DARKCAL APP [40,41], was developed to compute the image dark rate for various types of OMPS SDR data. For example, OMPS dark current measurements include two types, door-closed and door-open data. The door-closed data are collected during the night side of the orbit, with the sensor's entrance aperture blocked. This typically occurs over middle latitudes outside of the SAA area and is conducted once a week. The door-open data are measured over each orbit, thus having a risk of being contaminated by SAA transient pixels. In this study, we employ the same processing method as the DARKCAL APP to calculate the dark rate of the NOAA-21 OMPS NM based on door-open and door-closed measurements, used for the calibration of Earth radiance data. The computation procedures were also briefed in [14,17,39] based on the formulae provided in the DARKCAL APP. In this study, only the

computation formula for the dark (image region) rate at a pixel is given for understanding its principle. All subscripts in the involved variables are omitted for simplification.

$$D^{Obs} = n_{coadd} \cdot t_{Int}\, DR_{ImageRegion} \tag{10}$$

$$DR_{ImageRegion} = \frac{D_{IRegion} - D_{Readout} - D_{Smear}}{t_{IRS}} \tag{11}$$

In the above equations, $DR_{ImageRegion}$ denotes the dark image region rate, often referred to simply as the dark rate; $D_{IRegion}$ represents the average of transient-free dark counts in the image region; $D_{Readout}$ denotes the average of dark counts during the readout time in the storage region; D_{Smear} is the average of dark counts due to smear in the transition; t_{Int} denotes the integration time for the OMPS NM dark data image region; t_{Dwell} denotes the dwelling (readout) time for dark counts in the storage region; t_{IRS} is the exposure time of the dark count measurements. In addition, in the OMPS SDR processing, the dark count is binned according to the Earth-view (EV) sample table. For IDPS use, n_{coadd} = 100.

Figure 2a presents the time series of the NOAA-21 OMPS NM dark rate since the first dark count measurement, while Figure 2b shows the time series of the 'hot' pixel percentage. Here, the hot pixel in the measured dark counts is defined by using a pre-loaded hot pixel threshold, which is 8 sigma to the mean that is derived from the first orbit of the dark data. The dark rate gradually increases with time due to an accumulation of 'hot' pixels caused by radiation damage in the space environment [17], which is confirmed in Figure 2b. However, the gradually increased 'hot' pixel number only causes a small dark rate change: the average weekly change in the dark rate is approximately 0.01%. Especially, the accuracy of the radiance data at short wavelengths is very sensitive to changes in the dark rate. This is because Earth radiances are the lowest at short wavelengths, so that a given change in the dark rate is a larger fraction of the received overall signal at radiometric counts. The results shown in Figure 2a highlight the importance of routinely correcting the dark current in the OMPS SDR data calibration. Currently, in the operational processing, an updated dark rate table is routinely implemented into the IDPS operational procession for the OMPS SDR to capture changes in the dark rate over time due to increased 'hot' pixels.

It is noticed that, by comparing the results using the door-open and door-closed dark data in Figure 2a, the derived dark rates are comparable except for a 'routine' spike in the door-open-based dark rate (green line in the figure). These spikes are caused by monthly OMPS LED data measurements, which occur on Sunday every four weeks. For the NOAA-21 OMPS data, the dark calibration tables are delivered once a week by using Monday's door-open dark data. Thus, the spikes in the time series do not affect the performance of the delivered dark tables.

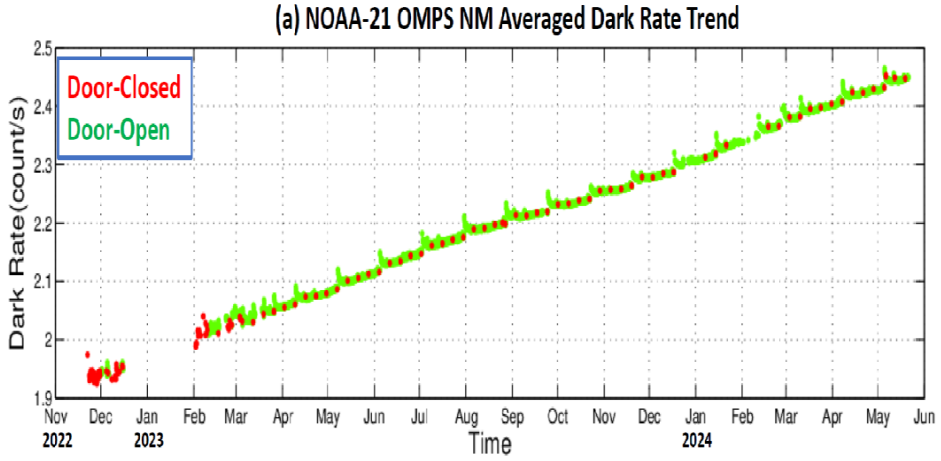


Figure 2. *Cont.*

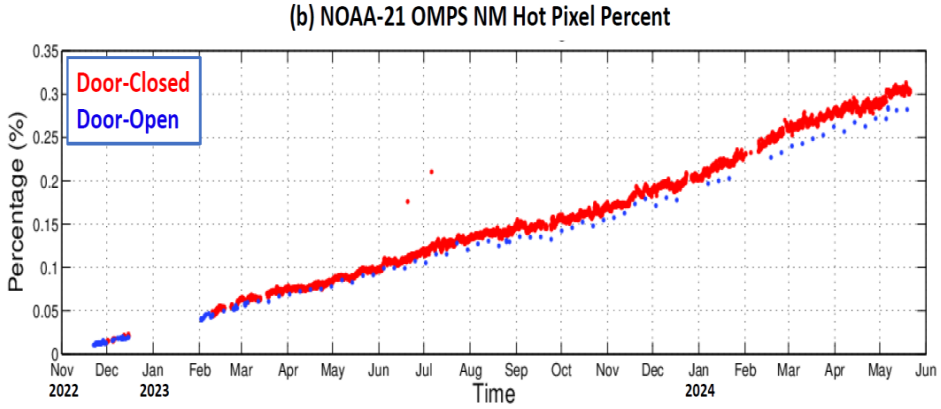


Figure 2. Time series of the NOAA-21 OMPS NM-averaged dark rate and hot pixel percent when the dark door is open and closed, separately. The data cover the period from 19 November 2022 to 27 May 2024. (**a**) Dark rate. (**b**) Hot pixel percent. The gaps in time series from 16 December 2022 to 2 February 2023 were caused by the KaTx-2 problem.

Additionally, updating the dark current from ground to in-orbit conditions is crucial. Our earlier analyses indicated that applying pre-launch dark current datasets to on-orbit NOAA-21 OMPS SDR data can cause anomalous features with striping patterns in the door-closed NOAA-21 OMPS NM and NP radiance data [28]. The caused differences are up to 1.5% in the NOAA-21 NM radiance at wavelengths below 303 nm, before and after applying an on-board dark rate calibration dataset (the figure is omitted). Therefore, a timely update in the IDPS operational procession for the OMPS SDR is essential. This includes updating the dark rate table from ground-based to in-orbit measurements and performing routine weekly updates of the dark rate tables. Such updates are necessary to capture changes in the dark rate due to instrument conditions and increases in 'hot' pixels over time. These timely updates can ensure the radiometric accuracy of the OMPS SDR data over time.

3.4. Wavelength Registration

The spectral wavelength registration determines instrument spectral wavelength shifts in on-orbit solar measurements in comparison with pre-launch defined baseline wavelength scales. It also includes regular updates to OMPS NM intra-orbit wavelength scales from time to time. Hence, this registration is performed with the following two steps: the one-time shift of the channel center wavelengths from ground to orbit and dynamic intra-orbit wavelength shift correction.

3.4.1. Wavelength Shift from Ground to Orbit

The ground-to-orbit wavelength shift is caused primarily by the rapid change in the OMPS instrument temperature from ground to orbit, which is a one-time shift. The shift can be estimated through minimization by adjusting the wavelengths of an on-orbit OMPS solar flux spectrum in early orbits until the total differences between the early on-orbit solar flux spectrum and a pre-launch synthetic solar spectrum across the entire OMPS NM wavelength range is minimized [18]. Here, the total difference between two solar spectra is expressed as follows [4,5,18]:

$$\chi^2(\Delta\lambda) = \sum_{\lambda=300nm}^{380nm} \left\{ \frac{F^{Mea}(\lambda+\Delta\lambda) - F^{Syn}(\lambda)}{F^{Syn}(\lambda)} \right\}^2 \tag{12}$$

$$F^{Syn}(\lambda) = \frac{\int_{\lambda-\Delta\lambda_0}^{\lambda+\Delta\lambda_0} F^{Ref}(\lambda') B\,(\lambda') d\lambda'}{\int_{\lambda-\Delta\lambda_0}^{\lambda+\Delta\lambda_0} B(\lambda') d\lambda'} \tag{13}$$

where $F^{Mea}(\lambda)$ represents the satellite-measured OMPS solar flux spectrum after performing Earth–sun distance correction and doppler correction due to satellite motion, and it is usually the initial OMPS solar flux measurement data used to mitigate the impact of on-orbit OMPS instrument degradation on the wavelength registration from ground to orbit; $F^{Syn}(\lambda)$ is the pre-launch synthetic solar spectrum, which is calculated using an extraterrestrial solar reference spectrum dataset convolved with the OMPS instrument bandpass function; $F^{Ref}(\lambda)$ is the extraterrestrial solar reference spectrum; $B(\lambda)$ denotes the instrument bandpass function at the central wavelength λ with a width of $\Delta\lambda_0$, which was measured in pre-launch measurements; the index of spatial resolution is omitted in each variable in Equations (9) and (10) for simplification. In this study, $F^{Ref}(\lambda)$ uses the solar flux atlas from ATLAS SUSIM [42,43] and Kitt Peak National Solar Observatory [44] in compliance with SNPP and NOAA-20 OMPS calibrations. Recently, another, more accurate, TSIS-1 Hybrid Solar Reference Spectrum has been recognized as a new solar irradiance reference standard [45,46], covering the OMPS nadir instrument wavelengths. It would be interesting to investigate its impact on OMPS SDR quality in future studies.

The initial NOAA-21 OMPS solar flux data using the working diffuser were measured on 2 September 2023. These data were utilized in the minimization of χ^2 in Equation (9) to derive a replacement for $F^{Mea}(\lambda)$ with specific wavelength shifts based upon the FOV position. This new solar spectrum is referred to as F^{Day1}, the day-1 solar spectrum. Figure 3a presents the averages of $F^{Mea}(\lambda)$, $F^{Day1}(\lambda)$, and $F^{Syn}(\lambda)$ across all FOV positions for the NOAA-21 OMPS NM SDR, denoted as $\overline{F^{Mea}(\lambda)}$, $\overline{F^{Day1}(\lambda)}$ and $\overline{F^{Syn}(\lambda)}$, respectively. The overall pattern of $\overline{F^{Mea}}$ closely resembles the pre-launch synthetic solar spectrum, while $\overline{F^{Day1}}$ is more comparable to $\overline{F^{Syn}}$ than $\overline{F^{Mea}}$, where λ is omitted for clarity. Figure 3b describes the NOAA-21 OMPS NM ground-to-orbit wavelength shift vs. the macropixel position. The sensor displays wavelength shifts ranging from -0.128 nm to -0.139 nm, with an asymmetric pattern around the nadir pixel position, particularly in the left off-nadir pixel area. These asymmetric features are related to goniometric non-uniform features within solar working diffuser (the figure is omitted).

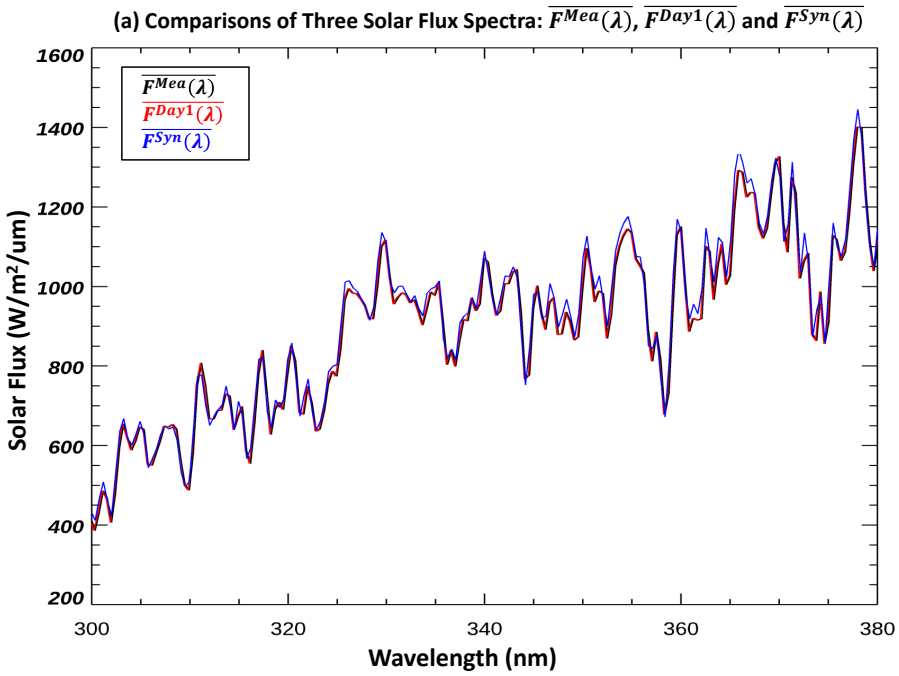


Figure 3. *Cont.*

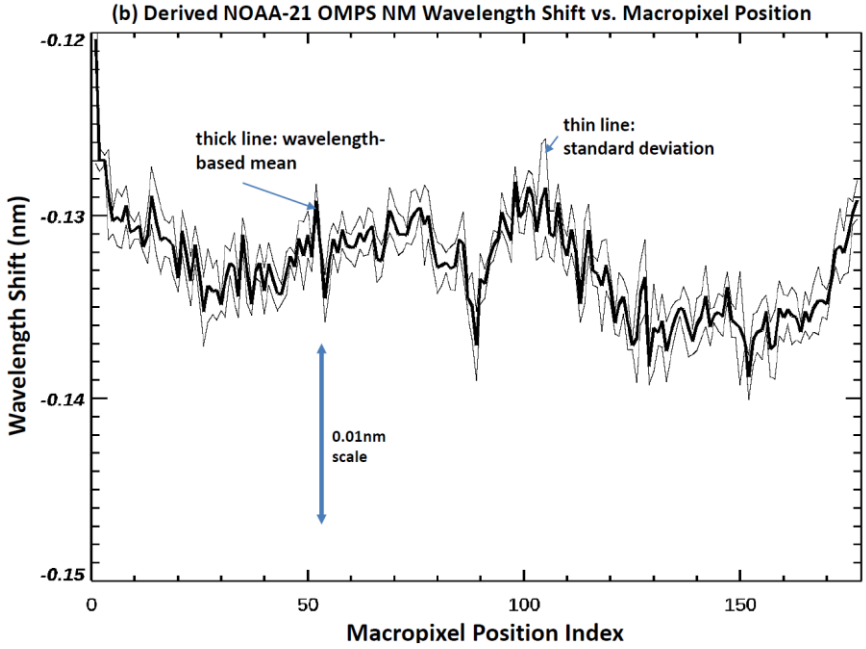


Figure 3. (**a**) Comparisons of three solar spectra for the NOAA-21 OMPS NM: $F^{Mea}(\lambda)$, $F^{Day1}(\lambda)$, and $F^{Syn}(\lambda)$. (**b**) Derived ground-to-orbit wavelength shifts as a function of the macropixel position. In (**b**), the thick line is the averaged wavelength shift at a given macropixel for all CCD micropixels within it, while the thin line is the standard deviation from the mean.

3.4.2. Intra-Orbit Wavelength Shift

After the OMPS instrument experiences a relatively large wavelength change from ground to orbit, it continues suffering from certain wavelength shifts with time due to the instrument temperature changes. Moreover, the OMPS NM in-flight wavelength shifts do not change monotonically with time. Earlier studies found that the SNPP OMPS NM SDR data experienced along-orbit wavelength shifts of more than 0.01 nm, exceeding the specification in Table 2. This phenomenon is caused by the OMPS NM housing and nadir calibration housing temperatures within an orbit cycle [7,18].

A similar intra-orbit wavelength shift occurs for the NOAA-21 OMPS NM SDR data due to the same reason. Figure 4 shows the time series of the NOAA-21 OMPS NM and nadir housing temperature differences and intra-orbit relative wavelength shift by using five orbits of data on 20 July 2024. The results in the figure show that large housing temperature differences (absolute value) result in relatively high wavelength shift. Here, the intra-orbit relative wavelength shifts are estimated by using an empirical algorithm in the current IDPS operational processing package. This algorithm was developed by adjusting the solar flux spectrum in the SDR solar table to the Earth wavelength scale as a function of latitude [7,47,48].

Figure 5 further compares the FOV-averaged intra-orbit wavelength scale vs. latitude for the SNPP, NOAA-20, and NOAA-21 OMPS NMs by using the entire day of data on 14 April 2024. The wavelength change range versus latitude represents the Earth radiance wavelength shift relative to the wavelength scales in the day-1 solar irradiances (i.e., F^{Day1}) provided in the SDR data. Generally, the NOAA-21 NM shows a stable intra-orbit wavelength shift pattern with a variation of 0.02 nm, which is smaller than that for either the NOAA-20 (~0.03 nm) or SNPP (~0.04 nm). In spite of smaller wavelength scale changes than the SNPP and NOAA-20, the wavelength shifts for the NOAA-21 exceeds the requirement if the shifts are not corrected. Like the SNPP and NOAA-20 OMPS NM SDR, therefore, the derived intra-orbit wavelength shifts have been applied into the operational IDPS processing for the NOAA-21 OMPS NM SDR to ensure that the wavelength scale accuracy is within the specification of $\pm$0.01 nm.

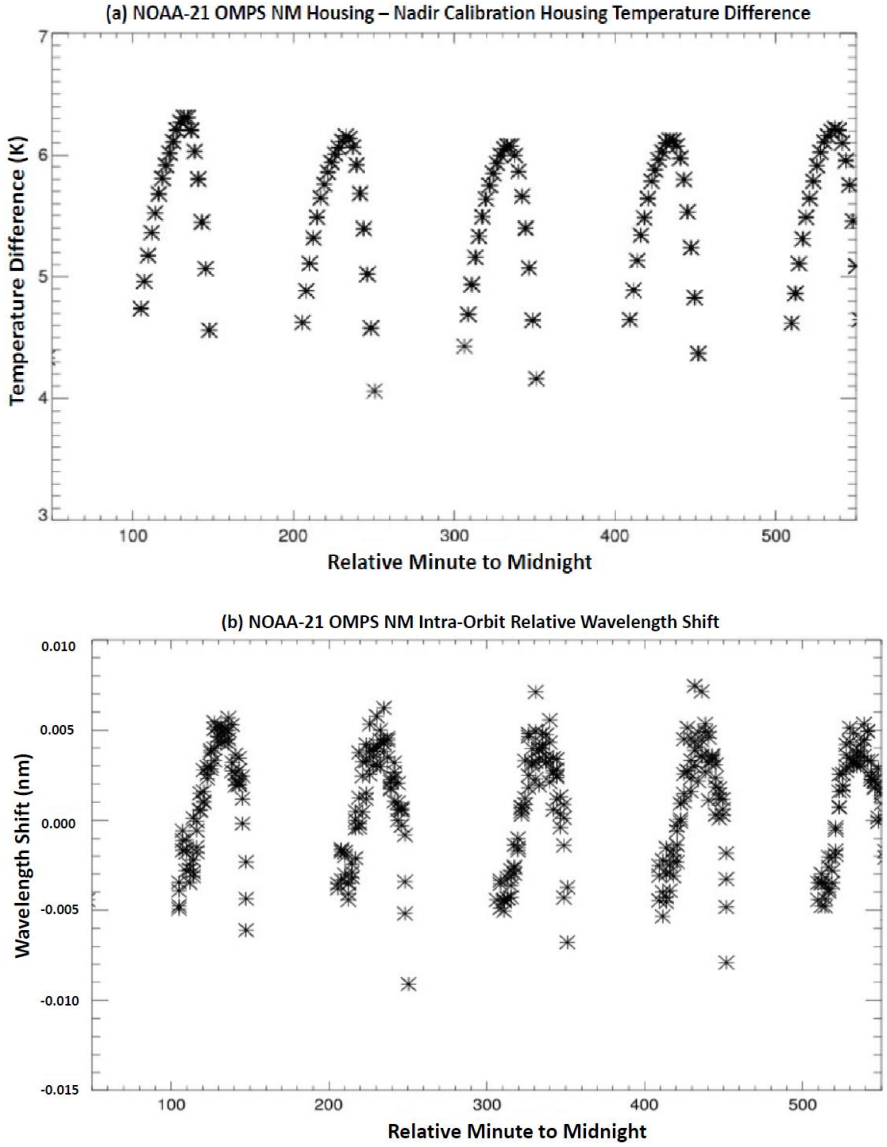


Figure 4. Time series of the NOAA-21 OMPS NM and nadir housing temperature differences and derived intra-orbit relative wavelength shift by using five orbits of data on 20 July 2024. (**a**) Instrument temperature difference. (**b**) Intra-orbit relative wavelength shift.

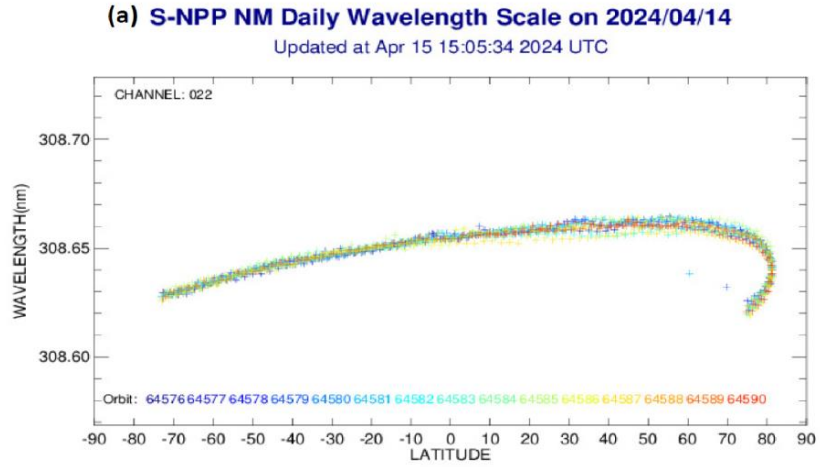


Figure 5. *Cont.*

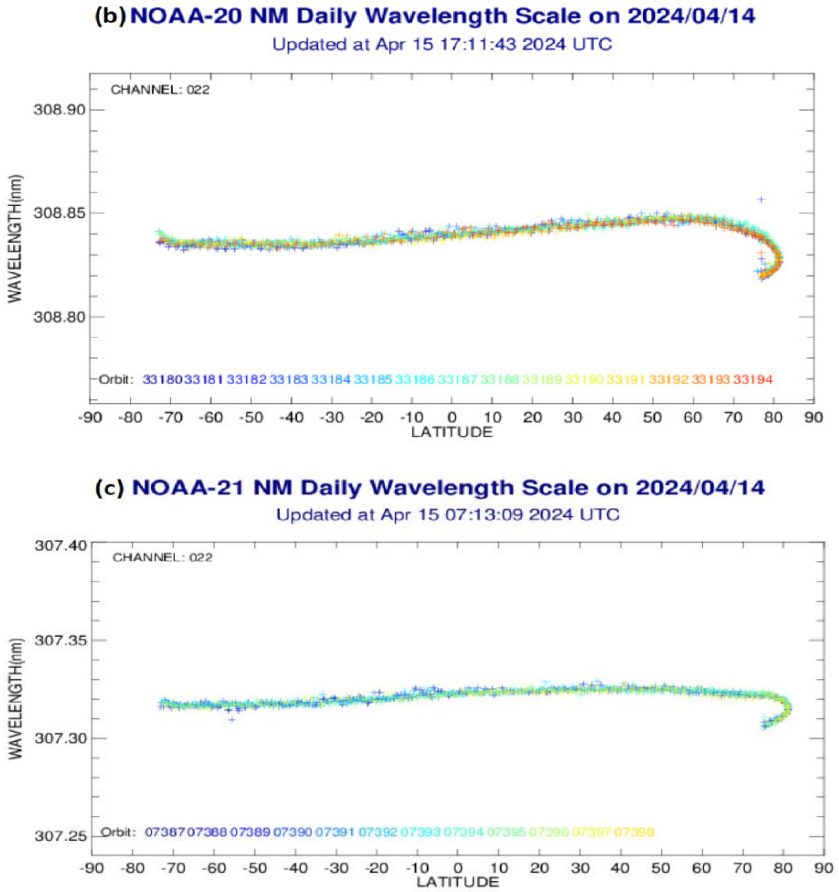


Figure 5. OMPS NM intra-orbit wavelength scale as a function of latitude by using the data on 14 April 2024 for the SNPP, NOAA-20, and NOAA-21. (**a**) SNPP; (**b**) NOAA-20; (**c**) NOAA-21.

3.5. Stray Light Correction

As a 2D spectral and spatial CCD detector, the OMPS NM is susceptible to internally scattered SL spectrally and spatially, the so-called OOF SL. The OOF SL is also defined as a signal within a spatial/spectral range originating from the same spectral band, but from outside of the convolution of the specular IFOV during a single measurement [5]. The following three possible sources can contribute to the OMPS OOF SL: off-axis scatter into the telescope's field-of-regard, scatter within the telescope (before the slit), and scatter within the spectrometer (after the slit) [5]. In addition to the OOF SL, for a given wavelength, the OMPS NM suffers from the OOB SL from other wavelengths. This is especially true for short wavelengths, since radiance magnitudes at longer wavelengths are much stronger than those at short wavelengths. The in-flight OMPS NM measures radiance up to approximately 410 nm, but in the IDPS operational processing system, the OMPS NM SDR data only cover the wavelength range up to 380 nm. Therefore, the OOF and OOB composite SL correction development in our operational calibration consists of the following two parts: the SL contribution below 380 nm and above 380 nm [5]. A detailed description of the OMPS NM SL correction was given in [20].

For the NOAA-21 OMPS NM, it uses a similar approach to that described in [5,20] to determine magnitudes of the OOF and OOB composite SL components based on the pre-launch OMPS NM instrument's PSF. In addition, an improved SL correction algorithm has been established in comparison with that in [5,20] to better quantify the contributions of the SL component above 380 nm. The development and performance assessment of the NOAA-21 OMPS NM SL correction algorithm will be covered in a separate manuscript [33]. The derived SL values have been implemented into the operational OMPS SDR processing system to remove the impact of the SL on the OMPS radiance.

Figure 6 illustrates the percentage of combined OOF and OOB SL components versus the wavelength for the NOAA-21 OMPS NM. The SL percentage is computed in comparison with radiance in the absence of SL correction, i.e., 100.0 × (radiance without SL correction-radiance with SL correction)/radiance without SL correction (%). The results demonstrate that the SL contribution is highly dependent upon the wavelength: large SL contributions up to 30% remain in the dichroic region from 300 to 310 nm, while the contributions are decreased to the order of 1% at wavelengths above 310 nm. The large stray light contributions below 310 nm are also due in part to the decrease in the absolute radiance signal.

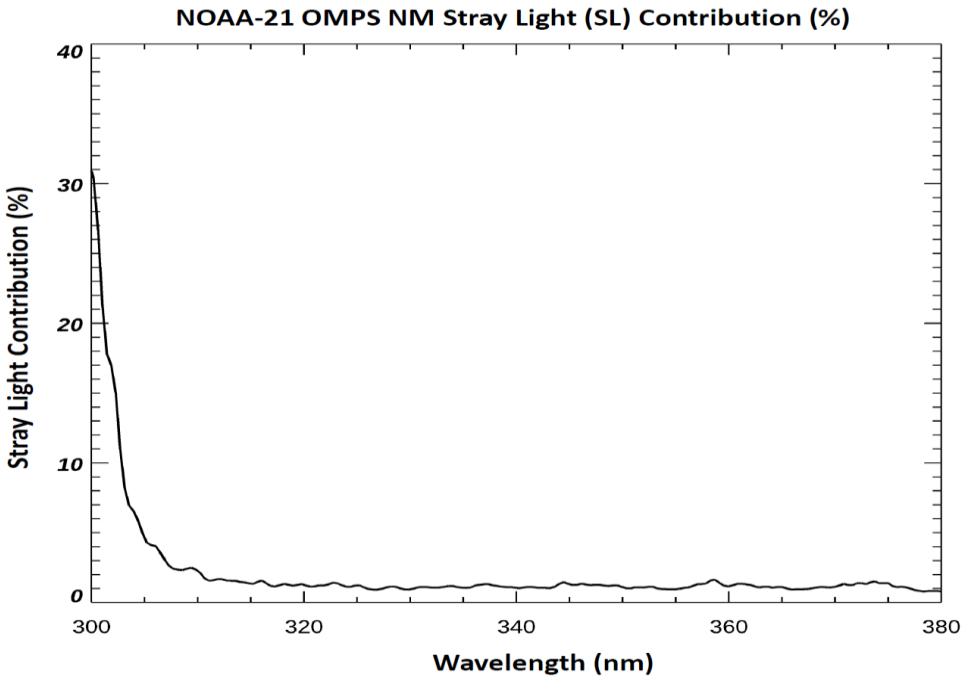


Figure 6. NOAA-21 OMPS NM stray light contributions as a function of the wavelength by using the newly derived stray light calibration coefficients. The computation was performed on the global data for solar zenith angles of less than 75°.

3.6. Geolocation Registration

Besides the spectral wavelength registration, the geolocation registration is another important calibration component. Through geolocation registration, the OMPS-NM LOS pointing vectors need to be mapped to geodetic longitude and latitude on the Earth's ellipsoid for each FOV at each scan position. It consists of two parts, the spacecraft-level algorithm and the sensor-specific algorithm. The spacecraft-level algorithm is commonly used by all instruments to compute the intersection of those LOS vectors with the Earth's ellipsoid to output geodetic longitude and latitude at a given UTC time, which was described in previous studies [49,50]. The geolocation registration in this study is only related to the sensor-specific geolocation algorithm.

The sensor-specific geolocation algorithm is designed to compute the pointing direction (unit vectors) of each individual CCD pixel in the OMPS instrument coordinates [5,25]. It also includes the alignment between the instrument and spacecraft coordinates via a field angle map calibration table, which was performed by using the pre-launch mounting matrix data. Hence, the post-launch analysis focuses on the computation of unit vectors. The OMPS NM unit vectors have been derived and expressed in the form of two rotational angles by the BATC, as described as follows [5]:

$$U_1 = sin\ sin\ (\beta) \quad (14)$$

$$U_2 = -sin\ sin\ (\alpha) \cdot sin\ sin\ (\beta) \quad (15)$$

$$U_3 = cos\ cos\ (\alpha) \cdot cos\ cos\ (\beta) \quad (16)$$

where α is the azimuth look angle (the rotation around the x-axis) and β is the elevation look angle (the rotation around the y-axis). Its coordinates were well illustrated in [5,25] so the descriptions are omitted here. The equations were supposed to be applicable for all OMPS NM instruments onboard the SNPP, NOAA-20, NOAA-21, and future JPSS-3 and JPSS-4 platforms.

However, the equations in Equations (8)–(10) were found to cause large geolocation errors of up to 90 km for off-nadir pixels in the SNPP and NOAA-20 OMPS NM SDR data [23,25,51]. The large geolocation errors were caused by a discrepancy in the OMPS instrument rotation coordinate definition between the ground and in-flight instrument systems (personal email communications with G. Jaross of NASA [52,53]). The unit vector equations defined in Equations (11)–(13) were expressed using an intrinsic rotation, i.e., the rotating azimuth look angle first before the rotating elevation look angle, which are consistent with that in the ground OMPS LOS measurement system. However, in-flight OMPS SDR measurements are made in an extrinsic rotation system. In this rotation system, the elevation look angle β is rotated first before the azimuthal angle α is rotated, which is opposite to that in the intrinsic rotation. As a result, the in-flight OMPS unit vectors need to be expressed by using the following equations (a personal email communication with G. Jaross of NASA in 2021, and [52,53]):

$$U_1 = cos\ cos\ (\alpha) \cdot sin\ sin\ (\beta) \quad (17)$$

$$U_2 = -sin\ sin\ (\alpha) \quad (18)$$

$$U_3 = cos\ cos\ (\alpha) \cdot cos\ cos\ (\beta) \quad (19)$$

The corrected equations have been applied to the IDPS operational processing system, which are applicable for OMPS instruments onboard the SNPP, NOAA-20, NOAA-21, and future JPSS-03 and JPSS-04 satellites. The geolocation accuracy for the NOAA-21 OMPS NM SDR with the corrected unit vector equations will be assessed against the VIIRS M1 band data in the following section.

4. Validation of NOAA-21 OMPS NM SDR Data Quality

The validation focuses on the NOAA-21 OMPS NM radiance, reflectance, and geolocation and Signal-to-Noise Ratio (SNR) performance using various approaches. For the radiometric performance, due to the lack of accurate reference, this study first employs two inter-sensor comparison methods to assess the performance of new SDR data relative to well-validated instrument observations which have the same or similar spectral and spatial resolutions. For the OMPS nadir instruments, the same type of instrument is flying on the SNPP, NOAA-20, and NOAA-21 platforms. Both the SNPP and NOAA-20 OMPS SDR have been well-calibrated and were demonstrated to meet the requirements defined in Table 2 [9,54,55]. Therefore, radiance and reflectance (or normalized radiance) in the NOAA-21 OMPS SDR are compared with those in the SNPP and NOAA-20. Two inter-sensor comparison approaches include the 32-day average method [34] and the CRTM-DD method, as described in Sections 4.1 and 4.2, correspondingly. In addition to the inter-sensor comparison approach, the deep convective cloud target is utilized to assess long-term stability of radiance data above 330 nm, as described in Section 4.3. The analyses of the geolocation and SNR performance are given in Sections 4.4 and 4.5, respectively.

4.1. NOAA-21 OMPS Radiance and Reflectance Differences Against SNPP or NOAA-20

The 32-day average method has been demonstrated to be able to provide reasonable averaged radiometric calibration biases between two instrument observations onboard two of the SNPP/NOAA-20 satellites. This is because this method uses two orbit-repeating cycles of data, such that the averaged differences have a relatively small diurnal impact [34].

To validate the performance of the NOAA-21 OMPS NM radiance data, Figure 7a displays the mean and standard deviation of a series of 32-day running-averaged radiance differences between the NOAA-21 and SNPP OMPS NM SDR datasets since 1 June 2023 through 12 December 2023. Here, the running 32-day average represents the differences in the data that are computed over a 32-day period, with the computation being repeated consecutively by shifting the start and end points of the 32-day window by one day at a time. According to the results in the figure, the mean radiance deviations from the SNPP are mostly within ±3%, with the largest values below 303 nm. Even in the presence of a 1% standard deviation, the NOAA-21 OMPS NM SDR data show the averaged radiance differences within ±4% above 303 nm, which are also within the requirement of 8%. Despite the averaged radiance differences exceeding 8% below 301 nm, the OMPS ozone retrieval does not utilize the NM SDR data in this range. Hence, the significant biases below 303 nm do not impact the quality of the ozone data.

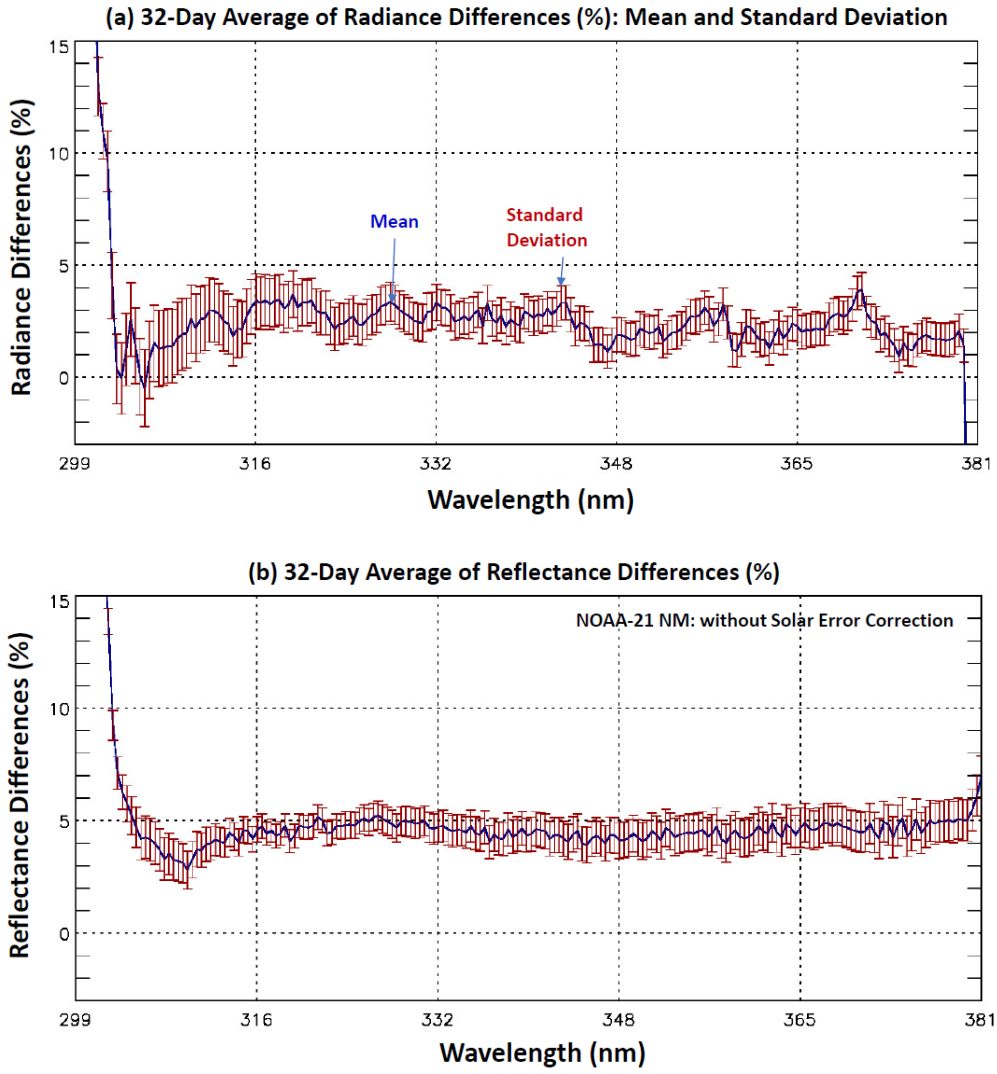


Figure 7. *Cont.*

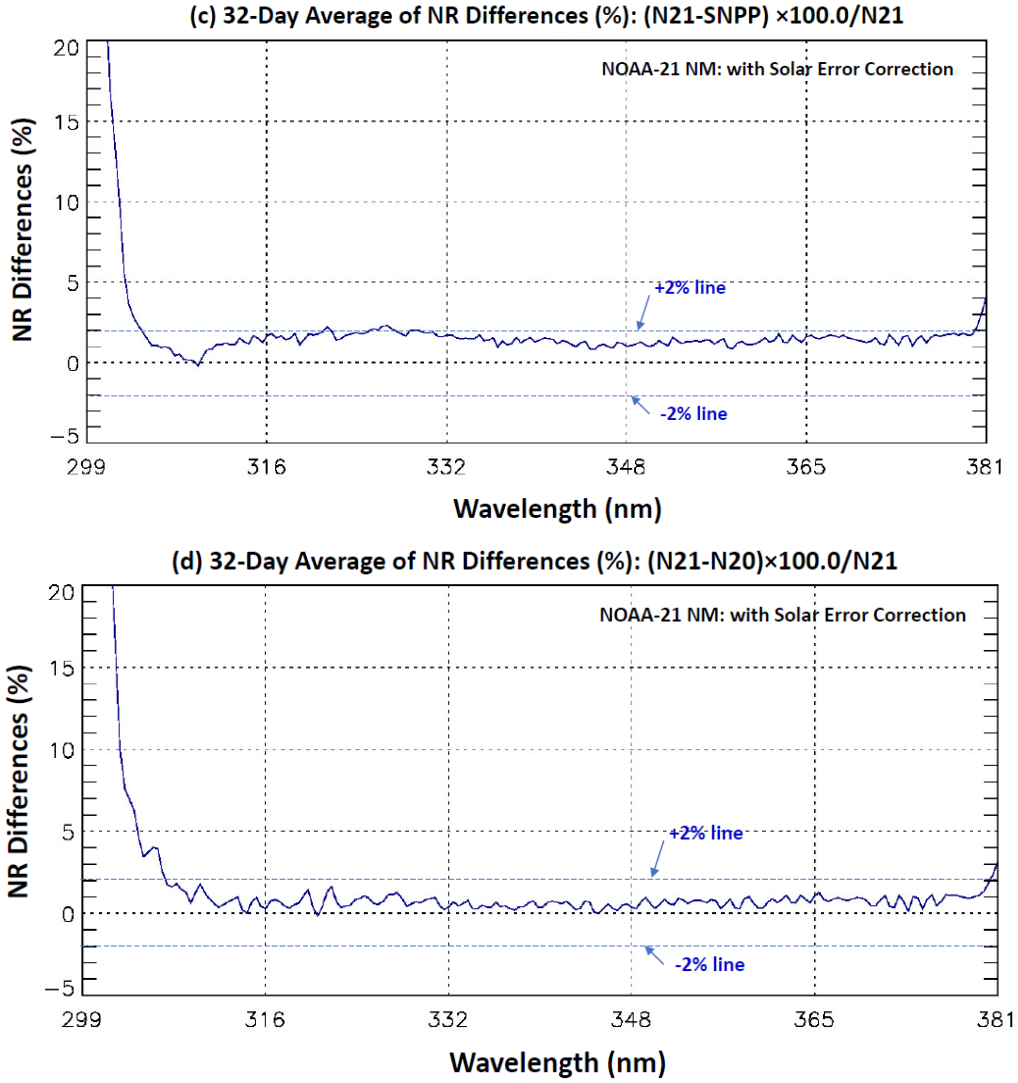


Figure 7. (**a**) Mean and standard deviation of a series 32-day running-average of radiance differences between the NOAA-21 and SNPP OMPS NM SDR datasets since 1 June 2023 through 12 December 2023. (**b**) Same as (**a**) but for reflectance. (**c**) The 32-day average of normalized radiance difference between the NOAA-21 and SNPP NM by using the NOAA-21 OMPS NM SDR dataset spanning from 15 May 2024 to 15 June 2024, where a correction of 2.2% has been applied. (**d**) Same as (**c**) but for the NOAA-21 and NOAA-20 OMPS NM.

To validate the performance of the NOAA-21 OMPS NM reflectance, Figure 7b presents a similar figure to (a) except for the reflectance. Note that the used SDR data in the figure do not include the correction of 2.2% for the NOAA-21 solar pre-launch calibration errors. The averaged reflectance differences between the NOAA-21 and SNPP NM vary in a range approximately from 3% to 4%, with exceptions below 303 nm, where the differences are the largest. If a correction of 2.2% is applied to the NOAA-21 NM solar flux data, the averaged reflectance differences above 303 nm will be decreased to levels below 2% (the figure is omitted). Figure 7c further illustrates 32-day average of normalized radiance differences using recent NOAA-21 OMPS NM SDR data spanning from 15 May 2024 to 15 June 2024, where the correction of 2.2% has been applied. We used normalized radiance here, since a similar comparison is made using the same period of the NOAA-21 dataset except that the NOAA-20 is used as a reference. Figure 7d displays the inter-sensor differences in the normalized radiance between the NOAA-21 and NOAA-20 NM by using the same period of datasets in Figure 7c. The averaged deviations are even smaller than those in Figure 7c, which are mostly within ±1% for the same wavelength range. The smaller NOAA-21

inter-sensor biases with the NOAA-20, compared to those with the SNPP, are partially related to the optical throughput degradation of the SNPP OMPS NM instrument [55].

Overall, the NOAA-21 OMPS SDR data are generally consistent in quality with the SNPP and NOAA-20 data. Two different references lead to a similar conclusion that radiometric calibration biases in the NOAA-21 OMPS NM SDR after the solar flux error correction are generally within ±2%, with margins in the range from 300 to 303 nm. This confirms the effectiveness of the empirical solar bias correction scale factor derived in Section 3.2.

4.2. OMPS Normalized Radiance Double Differences Between NOAA-21 and SNPP by Using CRTM as a Bridge

The 32-day average differences clearly demonstrate the good radiometric quality of the NOAA-21 OMPS NM data in radiance and reflectance (and normalized radiance) compared to either the SNPP or NOAA-20 data. Below, the inter-sensor radiometric calibration biases are further assessed using RTM simulation as a bridge, specifically by examining the double differences in the NOAA-21 and SNPP radiance (reflectance) deviations from the RTM simulations. Its principle can be expressed by the following equation:

$$\overline{DD}^{RTM}_{N21-SNPP} = \left(\overline{O} - \overline{B}\right)_{N21} - \left(\overline{O} - \overline{B}\right)_{SNPP} \quad (20)$$

where O and B denote satellite observations (radiance, normalized radiance, or reflectance) and RTM simulations, respectively; the subscript $N21$ and $SNPP$ are the NOAA-21 OMPS NM and SNPP OMPS NM, respectively; the bar '$-$' above each of O and B signifies the mean over selected observations; $\overline{DD}^{RTM}_{N21-SNPP}$ represents the average of the radiometric difference between the NOAA-21 and SNPP OMPS SDR data via the RTM. In this study, the RTM denotes the JCSDA CRTM, and its descriptions are referred to [12,56–58].

It is important to note that it is still challenging to conduct accurate RTM simulations due to the lack of cloud profile information. So, Equation (20) is only applied to satellite observations under clear skies. Even under clear skies, however, a few error sources can contribute to each of $(\overline{O} - \overline{B})$, e.g., instrument calibration errors (e.g., BPS difference, solar cal. error, and cal. algorithm error), RTM modeling errors (e.g., solar reference dataset difference), and simulation errors due to inaccurate inputs such as surface reflectivity or/and ozone profile. Approximately, the errors except for the first item would be mostly canceled through the double difference and average in Equation (20). Therefore, it is assumed that $\overline{DD}^{RTM}_{N21-SNPP}$ approximately represents the radiometric calibration differences between the NOAA-21 and SNPP.

Figure 8 shows a globally averaged NR difference as a function of the wavelength under clear skies by using the SNPP and NOAA-21 OMPS SDR data on 20 February 2024. The surface reflectivity uses the NOAA SNPP OMPS EDR products. Note that the bias correction of 2.2% has not been applied to the operational NOAA-21 OMPS SDR data until 11 April 2024. Thus, the results with the 2.2% correction are also included in the figure as a comparison. According to the results in the figure, the mean NR differences with the correction are mostly within ±2% at wavelengths above 305 nm, while the values without the correction are frequently above the 2% line. Similarly, large discrepancies remain at wavelengths below 303 nm, which are consistent with those using the 32-day average method in Figure 7 above. Even so, these large errors do not impact the quality of current ozone products, since the data below 303 nm are not used. Finally, small stripes remain at a few wavelengths, which might be associated with inconsistencies in the wavelength scale and bandpass spectral characteristics between the SNPP and NOAA-21. Further investigation is needed to better understand the root cause of the phenomenon in future studies.

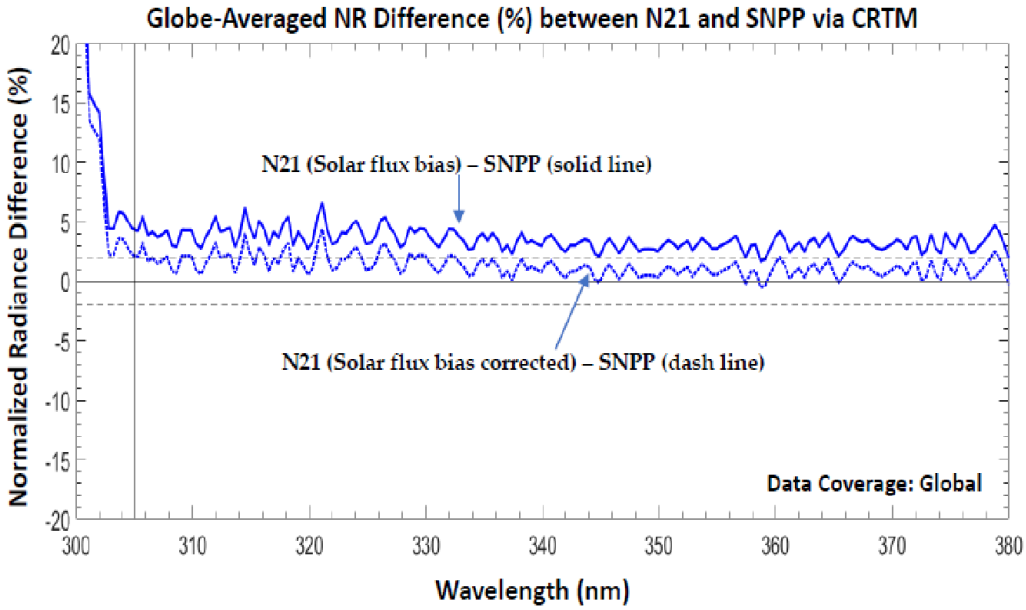


Figure 8. Averaged double differences in the normalized radiance under clear skies between the NOAA-21 and SNPP by using the data on 2 February 2024.

4.3. Long-Term Stability of NOAA-21 OMPS NM SDR Data

DCCs are the brightest tropical Earth targets located in a thin band near the equator called Inter-Tropical Convergence Zone [59]. DCC targets are approximately ideal visible calibration targets with nearly a Lambertian reflectance. Thus, in recent years, a new method associated with DCC targets was initialized to assess the stability of VIIRS SDR data [59,60]. This method has been successfully extended to SNPP OMPS NM SDR data. According to the analysis in [35,36], OMPS NM DCC pixels are identified by using the infrared threshold from collocated VIIRS brightness temperature measurements at the 10.729-μm band: the solar zenith angle is less than 40 degrees; the sensor view zenith angle is less than 35 degrees; the averaged brightness temperature (TB) from the collocated VIIRS pixels at channel M15 is less than a temperature threshold; the standard deviation of TB at M15 from the collocated VIIRS pixels is less than a spatial uniformity threshold. These criteria are similar to previous studies [59–61]. A detailed description about this analysis is referred to in [35,36].

Here, this method is applied to the NOAA-21 OMPS-NM SDR data to assess the stability of the OMPS NM reflectance within DCC targets at several wavelengths above 330 nm.

Figure 9 shows a one-year time series of NOAA-21 OMPS NM reflectance within DCC targets at several wavelengths above 331 nm. Large drops in reflectance after April 2024 are observed, which are caused by the updated solar flux table by 2.2% in the SDR data. Except for these drops, the averaged reflectance exhibits some variations with time, primarily due to solar angle differences and atmospheric feature changes with time. Nevertheless, the NOAA-21 OMPS-NM SDR data long-term reflectance within the DCC targets at the selected wavelengths is stable within 0.5% changes during this period. This demonstrates the good stability of the NOAA-21 OMPS NM SDR data, except for an update to the solar flux calibration table.

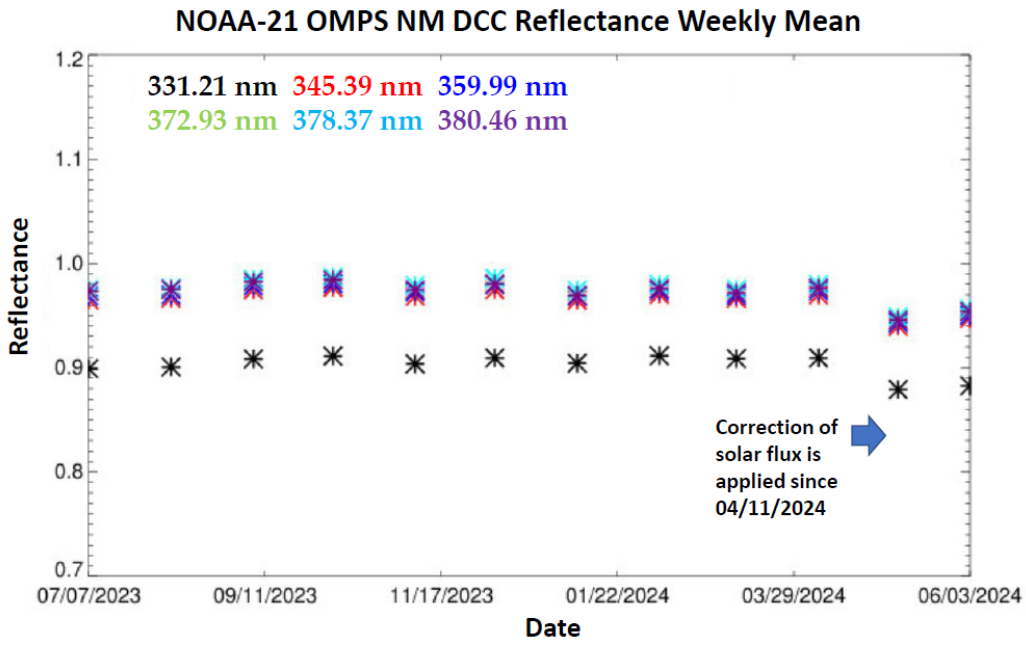


Figure 9. Time series of the NOAA-21 OMPS NM reflectance within the DCC targets from 7 July 2023, to 7 June 2024 at wavelengths of 331.21, 345.39, 359.99, 372.93, 378.37, and 380.46 nm. Only the first week of the data per month is used to produce an average to reduce the impact of different solar angles with time on the stability of the reflectance. Large drops in reflectance after April 2024 are caused by the updated solar flux table by 2.2% in the SDR data that was implemented into the IDPS operational system on 11 April 2024.

4.4. Geolocation Accuracy Assessment

A method was developed to efficiently assess the SNPP and NOAA-20 OMPS NM geolocation accuracy [25]. It utilizes spatially collocated radiance measurements from the VIIRS Moderate Band M01, with a central wavelength of 410 nm spanning from 400 to 420 nm. Its basic idea is to find the best collocation position, with a maximum correlation between the VIIRS collocated and real OMPS NM radiances. It is performed by perturbing the OMPS NM line-of-sight (LOS) vectors in the cross-track and along-track directions, with small steps in the spacecraft coordinates. The detailed description of the method is referred to in [25]. The NOAA-21 VIIRS SDR data geolocation has been well calibrated, with geolocation errors within a couple of hundreds of meters [62]. Therefore, this study uses the same method in [25] to assess the accuracy of the NOAA-21 OMPS NM SDR geolocation accuracy against the NOAA-21 VIIRS M1 band geolocation location.

Figure 10a,b present the geolocation accuracy of the NOAA-21 OMPS NM SDR data in both along-track and cross-track directions against the NOAA-21 VIIRS M1 band data by randomly selecting a day last year. In the computation, radiance at a wavelength of 380 nm, or the nearest available wavelength to 380 nm, is used, as radiance at 380 nm is not always available at each location due to the instrument wavelength shift within-orbit. It is found that the NOAA-21 OMPS data have a better geolocation accuracy in the cross-track direction than in the along-track direction. The geolocation distance errors in the along-track can be as large as 3 km, while the errors in the cross-track direction are typically within ± 1 km. In addition, the along-track angle errors are shifted approximately by $-0.1^\circ \sim -0.15^\circ$ depending on the position in the spatial direction. Figure 10c,d show time series of the LOS vector angle errors in the along-track and cross-track directions for two FOV positions (leftmost and nadir). We can draw similar conclusions to the above ones, which indicate the long-term stability of the NOAA-21 OMPS NM SDR data geolocation. Regarding the remaining systematic error in the order of 0.1° in the along-track direction, it can be corrected by using an updated field angle map (FAM) calibration table based on the

perturbation method in [25], which will be covered in a future plan. In spite of this small systematic error, the NOAA-21 OMPS NM SDR data have demonstrated to consistently meet the specification of 8.5 km.

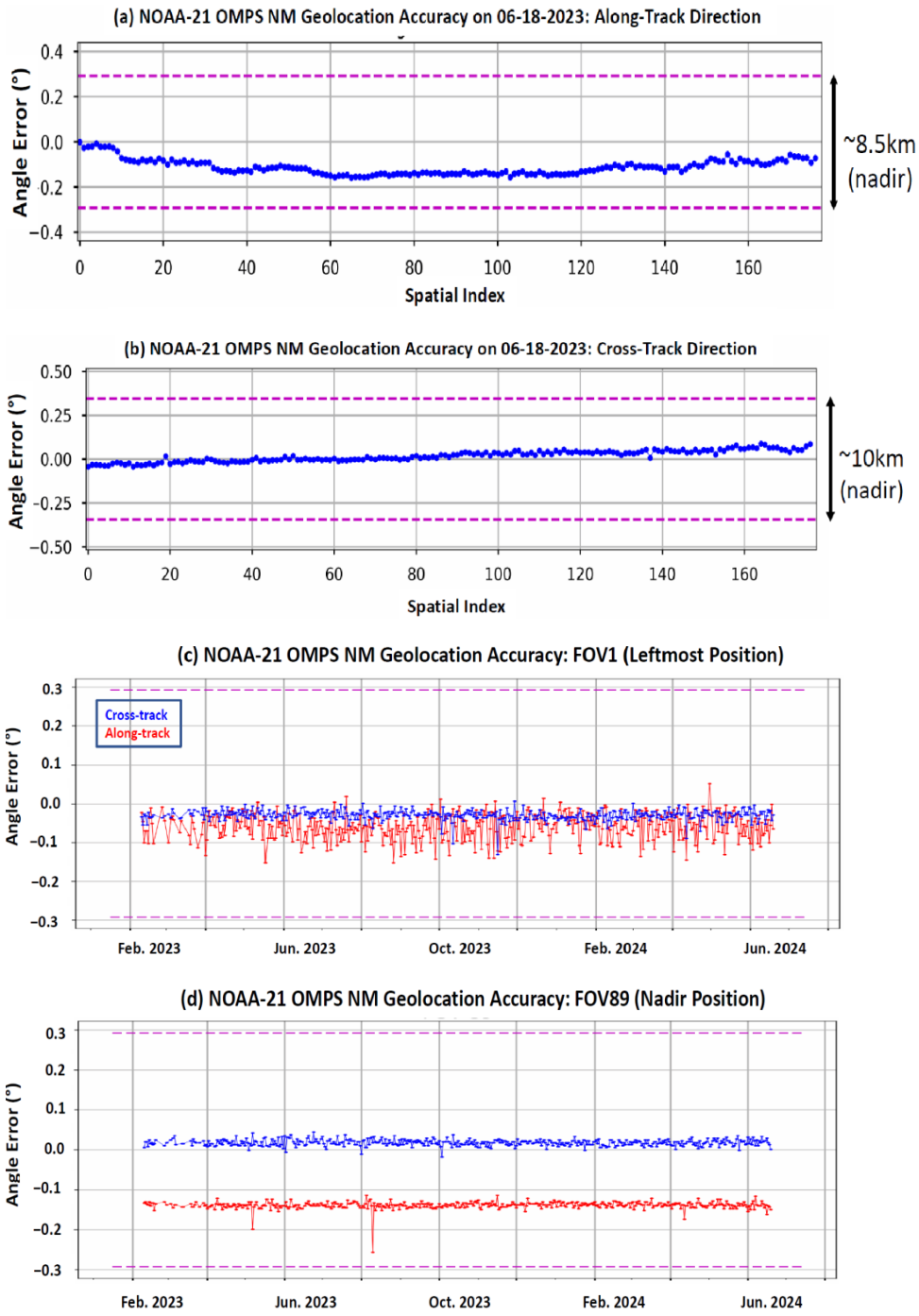


Figure 10. Geolocation accuracy of the NOAA-21 OMPS NM SDR data against the NOAA-21 VIIRS M1 band data geolocation position. (**a**) LOS vector angle error vs. spatial index in the along-track direction on 18 June 2023. (**b**) Same as (**a**) but in the cross-track direction. (**c**) Time series of the angle error at the leftmost pixel position in the spatial direction since 10 February 2023 through 20 June 2024. (**d**) Same as (**c**) but at the nadir pixel.

4.5. SNR Performance Assessment

As a precision term in radiometric calibration, SNR measures the strength of the desired signal relative to the background noise within instrument measurements. We com-

pute the SNR empirically based on root mean square residuals (RMSRs) for the observed radiance data. The estimation of the SNR is also an average over a certain wavelength range to reduce the impact of residual stray light and wavelength shift correction errors, e.g., 300–305, 305–325, 320–345, and 340–380. In addition, the SNR requirement in Table 2 is defined at a spatial resolution of 17 km at nadir, which is different from the actual NOAA-21 NM SDR nadir pixel resolutions, with 12 km in the cross-track and 10 km in the along-track directions. So, the obtained SNR values at the NOAA-21 pixel spatial resolution need to be converted into SNR values at 17 km × 17 km by multiplying by a scale factor of 1.54 $(=\sqrt{17/12 \times 17/10})$.

Figure 11a displays the derived SNR versus the wavelength for the NOAA-21 OMPS NM SDR data on 10 February 2023. As a comparison, the derived noise-corrected radiance and residuals (noise) are included in the figure. The NOAA-21 OMPS NM SDR data demonstrate good SNR performance within the requirement (green dashed line in the figure) for most of the wavelengths above 305 nm. Moreover, this performance is stable since launch, as shown in Figure 11b. Some exceptions at wavelengths above 305 nm should be related to the accuracy of the used empirical algorithm. Further study is needed to improve the performance of the SNR computation algorithm. Certainly, the data show poor SNR performance at wavelengths below 305 nm, which is mostly related to the dichroic effect. Due to this, the requirement for the SNR is defined only for wavelengths above 305 nm (see Table 2). Therefore, the SNR performance of the NOAA-21 OMPS NM SDR data meets the instrument requirement for the defined wavelengths. The small SNR values below 305 nm do not impact the quality of current ozone products.

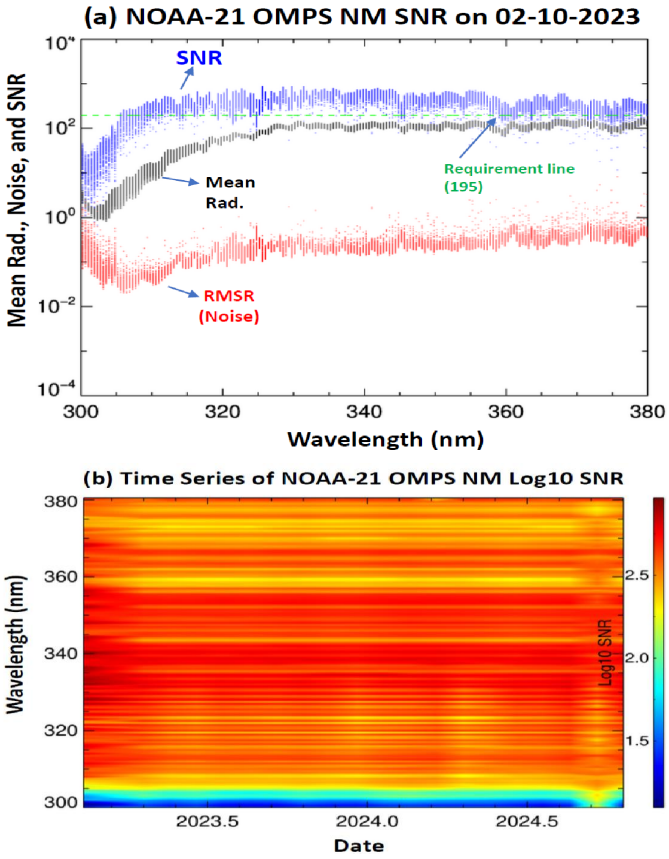


Figure 11. Estimated NOAA-21 OMPS NM data SNR using a root mean square residual (RMSR) analysis method. (**a**) Daily mean OMPS NM radiance SNR over tropical regions within [30°S, 30°N] on 10 February 2023, where the mean radiance and noise are added in the figure for a comparison. (**b**) Time series of the NOAA-21 OMPS NM SNR data from 1 April 2023 through 19 March 2024, using one day of data per week.

5. Summary and Conclusions

This study has updated/developed several key calibration algorithms/parameters for NOAA-21 OMPS NM SDR data to meet the JPSS scientific requirements. Those updated algorithms have been integrated into the IDPS processing system via either one-time or periodic calibration tables or code changes to generate quality-assured NOAA-21 OMPS NM SDR data. Furthermore, this study has validated the radiometric and geolocation performance of NOAA-21 OMPS NM SDR data using multiple methods. The results demonstrate that the quality of NOAA-21 OMPS NM SDR data is consistent with that of the SNPP and NOAA-20 OMPS data. It also meets the scientific requirements, with some exceptions primarily in the dichroic range between 300 nm and 303 nm. More details are described below.

Firstly, several calibration algorithms for the SNPP and NOAA-20 OMPS NM SDR are updated for the NOAA-21, including the dark current correction, one-time wavelength registration from ground to on-orbit, dynamic intra-orbit wavelength shift correction, and geolocation registration. In addition, an empirical scale factor of 2.2% is newly derived to mitigate pre-launch solar flux calibration errors, using a well-calibrated SNPP OMPS solar flux dataset as a reference. This factor is shown to effectively remove systematic errors in the NOAA-21 OMPS NM solar flux relative to both the SNPP and NOAA-20. Geolocation errors in the OMPS SDR off-nadir pixels, which potentially impacted all of the OMPS instruments, are effectively corrected in the NOAA-21 OMPS data by using the updated LOS unit vector equations that were given in previous studies for the SNPP and NOAA-20. Overall, those calibration algorithms offer a good performance for the NOAA-21 OMPS NM SDR data to meet the JPSS scientific requirements.

Secondly, the radiometric and geolocation accuracies of the NOAA-21 OMPS NM SDR data have been validated by using various approaches. For the radiance and reflectance or normalized radiance, two inter-sensor comparison methods, i.e., the 32-day average method and the CRTM-DD method, are employed to assess their accuracies relative to well-validated instrument observations from the SNPP and NOAA-20. The results show that the NOAA-21 OMPS NM SDR data are consistent with the SNPP and NOAA-20, with averaged differences mostly within $\pm$ 4% in radiance and 2% differences in reflectance (normalized radiance). Therefore, using two independent references, the NOAA-21 OMPS NM radiometric calibration accuracies in both radiance and reflectance are shown to generally meet the standards. Certain margins of errors remain in wavelengths below 303 nm. However, these discrepancies do not affect the quality of current ozone product retrievals, as the OMPS NM SDR data in this range are not utilized. Additionally, the DCC approach is employed to assess the stability of the NOAA-21 OMPS NM data. In the presence of solar angle differences, the changes in the NOAA-21 OMPS NM reflectance in a year is approximately 0.5%. For the geolocation accuracy, it is estimated using VIIRS M1 band data as a reference. The geolocation distance errors in the along-track can be as large as 3 km, while the errors in the cross-track direction are typically within $\pm$1 km. Both meet the requirement of being less than 8.5 km. The NOAA-21 OMPS NM SDR data also show a good SNR performance within the requirement. Overall, the NOAA-21 OMPS NM SDR data generally meet the required specifications for radiometric and geometric quality, although some margins remain in wavelengths below 303 nm.

In terms of the large radiometric calibration discrepancy below 303 nm, additional analyses should be conducted in future studies to improve the quality of the NOAA-21 OMPS NM SDR data in this range. Remaining errors in a few calibration parameters, such as solar flux and stray light, could contribute to this discrepancy. For example, according to our analysis, the NOAA-21 OMPS pre-launch calibration errors are highly wavelength-dependent, especially in the dichroic range. However, the current correction using a scale factor of 2.2% only accounts for a wavelength-independent or averaged error. In addition, the radiometric calibration accuracy of the NOAA-21 OMPS SDR data is evaluated in this study primarily using inter-sensor radiometric biases against both the SNPP and NOAA-20 observations, thus lacking an independent accuracy computation. The RTM simulation is

ideally an efficient approach to independently quantify radiometric calibration accuracy of the SDR data. This assumption is true if the information about atmospheric and surface properties is accurate, which is especially important for the OMPS NM data, since both accuracies of the simulated radiance and solar flux data are significantly sensitive to the accuracy of the surface reflectivity. Thus, another future study is to improve the accuracy of the CRTM simulations at the NM wavelengths, thus helping to improve the performance of the SL and solar flux error correction algorithms.

Author Contributions: Conceptualization, B.Y. and T.B.; methodology, B.Y., T.B., J.C., S.B., X.J., D.L., S.U., L.W., Q.L. and L.E.F.; software, B.Y., T.B., J.C., S.B., X.J., D.L., S.U., L.W., Q.L. and L.E.F.; validation, B.Y., T.B., J.C., S.B., X.J., S.U., J.H., Q.L., L.W. and W.D.P.; formal analysis, B.Y., T.B., J.C., S.B., X.J., D.L., S.U., J.H., L.W., Q.L. and W.D.P.; investigation, B.Y., T.B., J.C., S.B., X.J., S.U. and L.W.; resources, B.Y.; data curation, B.Y., T.B., J.C., S.B., X.J., S.U. and W.D.P.; writing, B.Y.; writing—review and editing, B.Y., S.U., S.B. and Q. Liu; visualization, J.C., S.B., X.J., S.U., L.W. and W.D.P.; supervision, B.Y.; project administration, B.Y.; funding acquisition, B.Y. All authors have read and agreed to the published version of the manuscript.

Funding: This study was sponsored by the JPSS program.

Data Availability Statement: The operational OMPS NM and NP SDR datasets are available in the NOAA Comprehensive Large Array-data Stewardship System (CLASS) by searching 'JPSS OMPS Sensor Data Record Operational (OMPS_SDR)'. The raw solar flux measurement data used in this study are provided in the NASA's Ozone Mapping and Profiler Suite (OMPS)'s SIPS.

Acknowledgments: Thanks to Chunhui Pan for her efforts in the NOAA-21 OMPS SDR pre-launch calibration preparation and for sharing knowledge and experiences in calibrating the OMPS SDR; thanks to Eric Beach for collecting OMPS SDR datasets within the STAR system. Thanks to Glen Jaross for sharing the pre-launch calibration coefficient datasets about the NOAA-21 with us; thanks to Glen Jaross, Colin Seftor, and Thomas Kelly for giving many valuable opinions during the work. Thanks to Manoharan Vani Starry and Bigyani Das for assisting in implementations of all NOAA-21 OMPS SDR calibration tables into the IDPS system. Thanks to Lihang Zhou and Ingrid Guch for giving valuable comments for the work at the JPSS mission level.

Conflicts of Interest: The authors declare no conflicts of interest.

Appendix A

Table A1. Acronyms used in this study.

Acronym	Description
OMPS	Ozone Mapping and Profiler Suite
NM	Nadir Mapper
NP	Nadir Profiler
VIIRS	Visible Infrared Imaging Radiometer Suite
RDR	Raw Data Record
SDR	Sensor Data Record
EDR	Environmental Data Record
SNO	Simultaneous Nadir Overpass
32D-AD	32-day Average Differences
JPSS	Joint Polar Satellite System
JPSS-01 (NOAA-20)	Joint Polar Satellite System-01
JPSS-02 (NOAA-21)	Joint Polar Satellite System-02
SNPP	Suomi National Polar-Orbiting Partnership

Table A1. *Cont.*

Acronym	Description
ICVS	Integrated Calibration/Validation System
SIPS	Science Investigator-led Processing System
PDA	Production, Distribution, and Access
IDPS	Interface Data Processing Segment
DCC	Deep Convective Cloud
CLASS	Comprehensive Large Array-Data Stewardship System
OOB	Out-of-Band
OOF	Out-of-Field
RTM	Radiative Transfer Model
CRTM	Community Radiative Transfer Model
CRTM-DD	Double-Difference (DD) Method via an RTM as a Vridge
FWHM	Full-Width at Half-Maximum
IFOV	Instantaneous Field-Of-View
CCD	Charge-143-Coupled Device
FFAs	Focal Plane Arrays
GRAVITE	Government Resources for Algorithm Verification, Independent Test, and Evaluation
SZA	Solar Zenith Angle
SAA	Southern Atlantic Anomaly
TSIS-1	Total and Spectral Solar Irradiance Sensor-1
UTC	Universal Time Coordinated
LOS	Line-of-Sight
SNR	Signal-to-Noise Ratio
RMSRs	Root Mean Square Residuals
LT	Long-Term
NRT	Near-Real-Time
STAR	Center for Satellite Application and Research
OSPO	Office of Satellite and Product Operations
ESPC	Environmental Satellite Processing Center
NWP	Numerical Weather Prediction
JCSDA	Joint Center of Satellite Data Assimilation
NOAA	National Oceanic and Atmospheric Administration

References

1. Dittman, M.G.; Ramberg, E.; Chrisp, M.; Rodriguez, J.V.; Sparks, A.L.; Zaun, N.H.; Hendershot, P.; Dixon, T.; Philbrick, R.H.; Wasinger, D. Nadir ultraviolet imaging spectrometer for the NPOESS Ozone Mapping and Profiler Suite (OMPS). In Proceedings of the International Symposium on Optical Science and Technology, Seattle, WA, USA, 24 September 2002; Volume 4814, Earth Observing Systems VII. [CrossRef]
2. Rodriguez, J.V.; Seftor, C.J.; Wellemeyer, C.G.; Chance, K. An overview of the nadir sensor and algorithms for the NPOESS Ozone Mapping and Profiler Suite (OMPS). *Proc. SPIE* **2003**, *4891*, 65–76.
3. Remund, Q.P.; Newell, D.; Rodriguez, J.V.; Asbury, S.; Jaross, G. The Ozone Mapping and Profiler Suite (OMPS): On-orbit calibration design. *Proc. SPIE* **2004**, *5652*, 165–173.
4. Joint Polar Satellite System (JPSS). *OMPS Nadir Profile Ozone Algorithm Theoretical Basis Document (ATBD)*; JPSS Ground Project Code 474-00026; Goddard Space Flight Center: Greenbelt, MD, USA, 2014.

5. Joint Polar Satellite System (JPSS). *OMPS NADIR Total Column Ozone Algorithm Theoretical Basis Document (ATBD)*; JPSS Ground Project Code 474-00029; Goddard Space Flight Center: Greenbelt, MD, USA, 2014.
6. Jaross, G.; Bhartia, P.K.; Chen, G.; Kowitt, M.; Haken, M.; Chen, Z.; Xu, P.; Warner, J.; Kelly, T. OMPS Limb Profiler instrument performance assessment. *J. Geophys. Res.* **2014**, *119*, 4399–4412. [CrossRef]
7. Flynn, L.; Long, C.; Wu, X.; Evans, R.L.; Beck, C.T.; Petropavlovskikh, I.; Mcconville, G.; Yu, W.; Zhang, Z.; Niu, J.; et al. Performance of the Ozone Mapping and Profiler Suite (OMPS) Products. *J. Geophys. Res. Atmos.* **2014**, *119*, 6181–6195. [CrossRef]
8. Flynn, L. Atmospheric Chemistry Products from the Ozone Mapping and Profiler Suite (OMPS) Validation and Applications. In Proceedings of the NOAA Satellite Conference 2015, Greenbelt, MD, USA, 27 April–1 May 2005.
9. Flynn, L.; Petropavlovskikh, I.; Long, C.; Beck, T.; Niu, J.; Beach, E.; Zhang, Z.; Caponi, M.; Sen, B. Science Maturity Review for OMPS Total Column Ozone EDR–V8TOz. August 2015. Available online: https://www.star.nesdis.noaa.gov/jpss/documents/AMM/NPP/OMPS_Ozone_TC_Val.pdf (accessed on 6 June 2022).
10. Flynn, L.; Petropavlovskikh, I.; Long, C.; Beck, T.; Niu, J.; Beach, E.; Zhang, Z.; Caponi, M.; Sen, B. Science Maturity Review for OMPS Total Column Ozone EDR–V8Pro. August 2015. Available online: https://www.star.nesdis.noaa.gov/jpss/documents/AMM/NPP/OMPS_Ozone_NP_Val.pdf (accessed on 1 September 2015).
11. Niu, J.; Flynn, L.E.; Beck, T.; Zhang, Z.; Beach, E. Evaluation and Improvement of the Near-Real-Time Linear Fit SO2 Retrievals from Suomi NPP Ozone Mapping and Profiler Suite. *IEEE Trans. Geosci. Remote Sens.* **2021**, *59*, 101–113. [CrossRef]
12. Liu, Q.; Cao, C.; Grassotti, C.; Liang, X.; Chen, Y. Experimental OMPS Radiance Assimilation Through One-Dimensional Variational Analysis for Total Column Ozone in the Atmosphere. *Remote Sens.* **2021**, *13*, 3418. [CrossRef]
13. Yan, B.; Pan, C.; Beck, T.; Jin, X.; Wang, L.; Liang, D.; Flynn, L.; Chen, J.; Huang, J.; Buckner, S.; et al. New Reprocessing Towards Life-Time Quality-Consistent Suomi NPP OMPS Nadir Sensor Data Records (SDR): Calibration Improvements and Impact Assessments on Long-Term Quality Stability of OMPS SDR Data Sets. *Remote Sens.* **2022**, *14*, 3125. [CrossRef]
14. Pan, C.; Kowalewski, M.; Buss, R.; Flynn, L.; Wu, X.; Caponi, M.; Weng, F. Performance and Calibration of the Nadir Suomi-NPP Ozone Mapping Profiler Suite from Early-Orbit Images. *IEEE J. Sel. Top. Appl. Earth Obs. Remote Sens.* **2013**, *6*, 1539–1551. [CrossRef]
15. Seftor, C.J.; Jaross, G.; Kowitt, M.; Haken, M.; Li, J.; Flynn, L.E. Postlaunch performance of the Suomi National Polar-orbiting Partnership Ozone Mapping and Profiler Suite (OMPS) nadir sensors. *J. Geophys. Res. Atmos.* **2014**, *119*, 4413–4428. [CrossRef]
16. Wu, X.; Liu, Q.; Zeng, J.; Grotenhuis, M.; Qian, H.; Caponi, M.; Flynn, L.; Jaross, G.; Sen, B.; Buss, R.H.; et al. Evaluation of the sensor data record from the nadir instruments of the Ozone Mapping Profiler Suite (OMPS). *J. Geophys. Res. Atmos.* **2014**, *119*, 6170–6180. [CrossRef]
17. Pan, C.; Flynn, L.; Buss, R.; Wu, X.; Yu, W.; Grotenhuis, M. Performance Monitoring of the S-NPP Ozone Mapping and Profiler Suite's Sensor Data Records. *IEEE J. Sel. Top. Appl. Earth Obs. Remote Sens.* **2014**, *7*, 1763–1770. [CrossRef]
18. Pan, C.; Flynn, L. Solar observation of Ozone Mapping and Profiler Suite nadir system during the first 3 years of on-orbit operation. *J. Appl. Remote Sens.* **2015**, *9*, 94095. [CrossRef]
19. Pan, C.; Weng, F.; Flynn, L. Spectral Performance and Calibration of the Suomi NPP OMPS Nadir Profiler Sensor. *Earth Space Sci.* **2017**, *4*, 737–745. [CrossRef]
20. Pan, C.; Zhou, L.; Cao, C.; Flynn, L.; Beach, E. Suomi-NPP OMPS Nadir Mapper's Operational SDR Performance. *IEEE Trans. Geosci. Remote Sens.* **2019**, *57*, 1015–1024. [CrossRef]
21. Pan, C.; Yan, B.; Cao, C.; Flynn, L.; Xiong, X.; Beach, E.; Zhou, L. Performance of OMPS Nadir Profilers' Sensor Data Records. *IEEE Trans. Geosci. Remote Sens.* **2020**, *59*, 6885–6893. [CrossRef]
22. Seftor, C.J.; Tiruchirapalli, R. SNPP/N20 NM OMPS Geolocation Analysis of error, Development of correction. In Proceedings of the NASA Ozone Processing Team (OPT) Meeting, Greenbelt, MD, USA, 7 July 2020.
23. Pan, C.; Yan, B.; Flynn, L.; Beck, T.; Wang, L.; Huang, J.; Huang, L. Recent Improvements to NOAA-20 Ozone Mapper Profiler Suit Nadir Profiler Sensor Data Records. In Proceedings of the IGARSS Virtual Conference, Brussels, Belgium, 12–16 July 2021.
24. Pan, C.; Flynn, L.; Wu, X.; Buss, R. Suomi National Polar-Orbiting Partnership Ozone Mapping Profiler Suite Nadir Instruments In-Flight Performance. *J. Appl. Remote Sens.* **2014**, *8*, 83499. [CrossRef]
25. Wang, L.; Pan, C.; Yan, B.; Beck, T.; Chen, J.; Zou, L.; Goldberg, M. A Method of Geolocation Assessment and Optimization for OMPS Nadir Mapper Using Visible Infrared Imaging Radiometer Suite (VIIRS). In Proceedings of the 102nd AMS Annual Meeting, Houston, TX, USA, 23–27 January 2022.
26. Yan, B.H.; Beck, T.; Chen, J.; Jin, X.; Jaross, G.; Buckner, S.; Huang, J.; Wang, L.; Uprety, S.; Liang, D.; et al. Provisional Maturity Science Review for OMPS Nadir Mapper and Nadir Profiler Sensor Data Record Algorithm (30 March 2023). Available online: https://www.star.nesdis.noaa.gov/jpss/documents/AMM/N21/NOAA-21_OMPS_Provisional.pdf (accessed on 15 April 2023).
27. Seftor, C.; Jaross, G. NOAA-21 OMPS Nadir Performance Status, JPSS OMPS SDR provisional maturity review. In Proceedings of the Virtual Meeting, 8800 Greenbelt Road, Greenbelt, MD, USA, 30 March 2023.
28. Yan, B.H.; Beck, T.; Chen, J.; Jin, X.; Jaross, G.; Buckner, S.; Huang, J.; Wang, L.; Uprety, S.; Liang, D.; et al. Beta Maturity Science Review for OMPS Nadir Mapper and Nadir Profiler Sensor Data Record Algorithm (23 February 2023). Available online: https://www.star.nesdis.noaa.gov/jpss/documents/AMM/N21/NOAA-21_OMPS_Beta.pdf (accessed on 15 March 2023).
29. Yan, B.H.; Beck, T.; Chen, J.; Jin, X.; Jaross, G.; Buckner, S.; Huang, J.; Wang, L.; Uprety, S.; Liang, D.; et al. Validated Maturity Science Review for OMPS Nadir Mapper and Nadir Profiler Sensor Data Record Algorithm (28 March 2024). Available online: https://www.star.nesdis.noaa.gov/jpss/documents/AMM/N21/NOAA-21_OMPS_Validated.pdf (accessed on 15 April 2024).

30. Yan, B.; Buckner, S.; Uprety, S.; Chen, J.; Beck, T.; Liang, D.; Flynn, L.; Manoharan, S. Assessing Calibration Errors in NOAA-21 OMPS NM and NP Solar Flux Relative to SNPP. In Proceedings of the NOAA JPSS Discrepancy Report Action Team (DRAT) Weekly Meeting, Virtual, 20 March 2024.
31. Lauderdale, J. *Joint Polar Satellite System (JPSS) Program Multi Mission System Specification (MMSS) Level 2 Requirements*; JPSS-REQ-1005/470-00101, Version 3.0 Joint Polar Satellite System (JPSS) Code 470; Goddard Space Flight Center: Greenbelt, MD, USA, 2020.
32. *Joint Polar Satellite System (JPSS) Level 1 Requirements Document Supplement (L1RDS)—Final*; JPSS-REQ-1002/470-00032, Revision 2.11, Joint Polar Satellite System (JPSS) Code 472; Goddard Space Flight Center: Greenbelt, MD, USA, 2019. Available online: https://www.nesdis.noaa.gov/s3/2022-03/L1RDS.pdf (accessed on 1 August 2023).
33. Chen, J.; Yan, B.; Beck, T. Stray light correction in NOAA-21 OMPS NM SDR: Improvement and Performance Assessment. *Remote Sens.* 2025; *submitted*.
34. Yan, B.; Goldberg, M.; Jin, X.; Liang, D.; Huang, J.; Porter, W.; Sun, N.; Zhou, L.; Pan, C.; Iturbide-Sanchez, F.; et al. A New 32-Day Average-Difference Method for Calculating Inter-Sensor Calibration Radiometric Biases Between SNPP and NOAA-20 Instruments Within ICVS Framework. *Remote Sens.* **2021**, *13*, 3079. [CrossRef]
35. Liang, D.; Yan, B.; Flynn, L.; Beck, T.; Sun, N.; Huang, J.; Jin, X. Feasibility analysis of OMPS NM SDR data long-term stability assessment using deep convective cloud targets, In Proceedings of the 2023 IEEE International Geoscience and Remote Sensing Symposium, Pasadena, CA, USA, 16–21 July, 2023.
36. Liang, D.; Yan, B.; Beck, T.; Flynn, L. SNPP OMPS NM SDR data long-term stability assessment using deep convective cloud targets. *Remote Sens.* 2025; *submitted*.
37. Peyush, J.; Gyanesh, C. 2015: Overview of the JPSS GRAVITE System, 2015 JPSS Annual Review. Available online: https://www.star.nesdis.noaa.gov/star/documents/meetings/2015JPSSAnnual/dayFive/04_Session8_Jain_GRAVITE%20Overview.pdf (accessed on 26 August 2015).
38. McNitt, J. 2017: Overview of NOAA NESDIS Direct Readout Services. Available online: https://www.ssec.wisc.edu/meetings/cspp/2017/presentations/day2/6_CSPP%20Users_McNitt_062617.pdf (accessed on 6 June 2022).
39. Pan, C.; Weng, F.; Jaross, G.; Wu, X.; Haken, M.; Flynn, L.; Janz, S.; Caponi, M.; Kowalewski, M.; Buss, R. OMPS Early Orbit Dark and Bias Evaluation and Calibration. In Proceedings of the 2012 IEEE International Geoscience and Remote Sensing Symposium, Munich, Germany, 22–27 July 2012; pp. 1092–1095. [CrossRef]
40. Haken, M. NASA Dark Current, Linearity, and Transients Calibration/Correction for OMPS Nadir Sensors. In Proceedings of the 2014 JPSS Annual Science Team Meeting, NOAA Center for Weather and Climate Prediction Conference Center, 5830 University Research Court, College Park, MD, USA, 12–16 May 2014. Available online: https://www.star.nesdis.noaa.gov/star/documents/meetings/2014JPSSAnnual/dayTwo/02_Session4c_Haken.pdf (accessed on 1 June 2014).
41. Haken, M. OMPS PEATE Dark Current Correction Algorithm, NASA OMPS PEATE, 2014.
42. Woods, T.N.; Prinz, D.K.; Rottman, G.J.; London, J.; Crane, P.C.; Cebula, R.P.; Hilsenrath, E.; Brueckner, G.E.; Andrews, M.D.; White, O.R.; et al. Validation of the UARS solar ultraviolet irradiances: Comparison with the ATLAS 1 and 2 measurements. *J. Geophys. Res. Atmos.* **1996**, *101*, 9541–9569. [CrossRef]
43. Brueckner, G.E.; Edlow, K.L.; Floyd, L.E.; Lean, J.L.; VanHoosier, M.E. The Solar Ultraviolet Spectral Irradiance Monitor (SUSIM) experiment on board the Upper Atmosphere Research Satellite (UARS). *J. Geophys. Res.* **1993**, *98*, 10695–10711. [CrossRef]
44. Kurucz, R.L.; Furenlid, I.; Brault, J.; Testerman, L. *Solar Flux Atlas from 296 to 1300 nm*; National Solar Observatory: Sunspot, NM, USA, 1984; p. 240.
45. Coddington, O.; Richard, E.; Harber, D.; Pilewskie, P.; Woods, T.N.; Chance, K.; Liu, X.; Sun, K. The TSIS-1 hybrid solar reference spectrum (Science Results from NASA's Solar Irradiance Science Team #2 (SIST-2)). *Geophys. Res. Lett.* **2021**, *48*, e2020GL091709. [CrossRef]
46. Coddington, O.M.; Richard, E.C.; Harber, D.; Pilewskie, P.; Woods, T.N.; Snow, M.; Chance, K.; Liu, X.; Sun, K. Version 2 of the TSIS-1 Hybrid Solar Reference Spectrum and Extension to the Full Spectrum. *Earth Space Sci.* **2023**, *10*, e2022EA002637. [CrossRef]
47. Flynn, L. OMPS Nadir Mapper Wavelength Shift Adjustment for Earth-View Measurements. In Proceedings of the NOAA JPSS Discrepancy Report Action Team (DRAT) Weekly Meeting, Virtual, 19 August 2013.
48. Joint Polar Satellite System (JPSS). *Joint Polar Satellite System Algorithm Specification Volume III: Operational Algorithm Description (OAD) for the OMPS Total Column RDR/SDR*; Joint Polar Satellite System (JPSS) Code 474, 474-00448-03-04, Revision A; Goddard Space Flight Center: Greenbelt, MD, USA, 9 August 2023.
49. Joint Polar Satellite System (JPSS). *VIIRS Geolocation Algorithm Theoretical Basis Document (ATBD)*; Joint Polar Satellite System (JPSS) Ground Project, Code 474, 474-00053; Goddard Space Flight Center: Greenbelt, MD, USA, 2011. Available online: https://lpdaac.usgs.gov/documents/135/VNP03_ATBD.pdf (accessed on 1 October 2012).
50. JPSS Configuration Management Office. *Joint Polar Satellite System (JPSS) Algorithm Specification Volume I: Software Requirement Specification (SRS) for Common Geolocation and Spacecraft Orientation*; Joint Polar Satellite System (JPSS) Code 474, 474-00448-01-08, Revision M; Goddard Space Flight: Greenbelt, MD, USA, 2022. Available online: https://www.nesdis.noaa.gov/s3/2023-08/474-00448-01-08_JPSS-SRS-Vol-I-Part-08_M.pdf (accessed on 15 April 2022).
51. Seftor, C.; Tiruchirapalli, R. SNPP/N20 NM OMPS Geolocation: Analysis of error, Development of correction, Results after application of correction. In Proceedings of the NASA Ozone Processing Team (OPT) Meeting, Greenbelt, MD, USA, 21 June 2020.

52. Wang, L.; Yan, B.; Pan, C.; Beck, T.; Chen, J. Root Cause Investigation and "Solution" for SNPP and NOAA-20 OMPS Nadir Mapper Off-Nadir Geolocation Error Issue. In Proceedings of the JPSS NOAA JPSS Discrepancy Report Action Team (DRAT) Weekly Meeting, Virtual, 2 December 2021. ADR00009633.
53. Yan, B.; Beck, T.; Wang, L.; Pan, C. OMPS Nadir Mapper Geolocation Code Change: Background, Changes, Verifications and Validations. In Proceedings of the JPSS NOAA JPSS Discrepancy Report Action Team (DRAT) Weekly Meeting, Virtual, 2 December 2021; ADR00009633.
54. Yan, B.H.; Beck, T.; Pan, C.; Xiong, X.; Devaliere, E. Validated Maturity Science Review for NOAA-20 OMPS Nadir Mapper and Nadir Profiler Sensor Data Record Algorithm (20 September 2019). Available online: https://www.star.nesdis.noaa.gov/jpss/documents/AMM/N20/OMPS_TC_SDR_Validated.pdf (accessed on 29 November 2019).
55. Pan, C.; Yan, B.; Flynn, L.; Beck, T.; Huang, J. Stability assessment for Sumi-NPP OMPS and NOAA-20 OMPS. In Proceedings of the GSICS Annual Virtual Meeting, College Park, MD, USA, 1 April 2021.
56. Chen, Y.; Weng, F.; Han, Y.; Liu, Q. Validation of the Community Radiative Transfer Model by Using CloudSat Data. *J. Geophys. Res. Atmos.* **2008**, *113*, D8. [CrossRef]
57. Ding, S.; Yang, P.; Weng, F.; Liu, Q.; Han, Y.; van Delst, P.; Li, J.; Baum, B. Validation of the community radiative transfer model. *J. Quant. Spectrosc. Radiat. Transf.* **2021**, *112*, 1050–1064. [CrossRef]
58. Liu, Q.; Yan, B.; Garrett, K.; Ma, Y.; Liang, X.; Huang, H.; Wang, W.; Cao, C. Deriving Surface Reflectance From Visible/Near Infrared and Ultraviolet Satellite Observations Through the Community Radiative Transfer Model. *IEEE J. Sel. Top. Appl. Earth Obs. Remote Sens.* **2022**, *15*, 2004–2021. Available online: https://ieeexplore.ieee.org/stamp/stamp.jsp?arnumber=9707621 (accessed on 1 December 2023). [CrossRef]
59. Doelling, D.R.; Morstad, D.; Scarino, B.R.; Bhatt, R.; Gopalan, A. The Characterization of Deep Convective Clouds as an Invariant Calibration Target and as a Visible Calibration Technique. *IEEE Trans. Geosci. Remote Sens.* **2013**, *51*, 1147–1159. [CrossRef]
60. Wang, W.; Cao, C. Assessing the VIIRS RSB calibration stability using deep convective clouds (Earth Observing Missions and Sensors: Development, Implementation, and Characterization III). *SPIE Asia-Pac. Remote Sens.* **2014**, *9264*, 11. [CrossRef]
61. Hu, Y.; Wielicki, B.A.; Yang, P.; Stackhouse, P.W.; Lin, B.; Young, D.F. Application of deep convective cloud albedo observation to satellite-based study of the terrestrial atmosphere: Monitoring the stability of spaceborne measurements and assessing absorption anomaly. *IEEE Trans. Geosci. Remote Sens.* **2004**, *42*, 2594–2599.
62. Cao, C.; Blonski, S.; Wang, W.; Shao, X.; Choi, T.; Zhang, F.; Bai, Y.; Ahmad, K.; Pillai, P.; Liu, T.; et al. Validated Maturity Science Review for NOAA-21 VIIRS Sensor Data Record Algorithm (3 August 2023). Available online: https://www.star.nesdis.noaa.gov/jpss/documents/AMM/N21/NOAA-21_VIIRS_Validated.pdf (accessed on 1 August 2023).

Disclaimer/Publisher's Note: The statements, opinions and data contained in all publications are solely those of the individual author(s) and contributor(s) and not of MDPI and/or the editor(s). MDPI and/or the editor(s) disclaim responsibility for any injury to people or property resulting from any ideas, methods, instructions or products referred to in the content.